Search for T-violating transverse muon polarization in the $K^+ \rightarrow \pi^0 \mu^+ \nu$ decay

M. Abe,[1,3] M. Aliev,[2] V. Anisimovsky,[2] M. Aoki,[3,4,*] Y. Asano,[1] T. Baker,[5] M. Blecher,[6] P. Depommier,[7] M. Hasinoff,[8] K. Horie,[3,4,*] Y. Igarashi,[3] J. Imazato,[3,†] A. P. Ivashkin,[2] M. M. Khabibullin,[2] A. N. Khotjantsev,[2] Yu. G. Kudenko,[2] Y. Kuno,[4] K. S. Lee,[9] A. Levchenko,[2] G. Y. Lim,[9,3,*] J. A. Macdonald,[10,‡] O. V. Mineev,[2] N. Okorokova,[2] C. Rangacharyulu,[5] S. Shimizu,[4] Y.-H. Shin,[11] Y.-M. Shin,[5,10] K. S. Sim,[9] N. Yershov,[2] and T. Yokoi[3]

(KEK-E246 Collaboration)

[1]*Institute of Applied Physics, University of Tsukuba, Ibaraki 305-0006, Japan*
[2]*Institute for Nuclear Research, Russian Academy of Sciences, Moscow 117312, Russia*
[3]*IPNS, High Energy Accelerator Research Organization (KEK), Ibaraki 305-0801, Japan*
[4]*Department of Physics, Osaka University, Osaka 560-0043, Japan*
[5]*Department of Physics, University of Saskatchewan, Saskatoon, Canada S7N 5E2*
[6]*Department of Physics, Virginia Polytechnic Institute and State University, Virginia 24061-0435, USA*
[7]*Laboratoire de Physique Nucléaire, Université de Montréal, Montréal, Québec, Canada H3C 3J7*
[8]*Department of Physics and Astronomy, University of British Columbia, Vancouver, Canada V6T 1Z1*
[9]*Department of Physics, Korea University, Seoul 136-701, Korea*
[10]*TRIUMF, Vancouver, British Columbia, Canada V6T 2A3*
[11]*Department of Physics, Yonsei University, Seoul 120-749, Korea*

At the 12-GeV proton synchrotron of KEK, an experiment (KEK-PS-E246) was performed to measure the transverse muon polarization (P_T) in $K^+ \rightarrow \pi^0 \mu^+ \nu$ decays as a direct search of violation of time reversal invariance (T-violation). P_T is a very sensitive probe of CP violation beyond the standard model. A stopped positive kaon beam was used. An elaborate high-acceptance detector, in conjunction with a 12-sector superconducting toroidal spectrometer, was utilized. The stopped kaon method provided several advantages in performing a high-precision experiment. The decay was identified by detecting a μ^+ with the spectrometer and a π^0 with a CsI(Tl) calorimeter surrounding the target as two photons as well as one photon with high energy. For the P_T measurement, π^0 events in the forward (*fwd*) and backward (*bwd*) regions in the calorimeter were relevant. Systematic errors were greatly suppressed by exploiting the rotational and *fwd-bwd* symmetry of the system. Polarization measurement was done in terms of asymmetry measurement of decay positrons of stopped muons in the polarimeter. A longitudinal field method was applied for the P_T polarization component. In the data analysis a novel technique of the two-analysis method was employed. Two independent analyses were performed following their own policy and criteria and good events were selected. Then, the two analyses were combined. A data quality check was carefully done by looking at the null asymmetry A_0, the sensitivity function A_N, the kinematical attenuation coefficient, and the decay-plane distributions. The asymmetry measurement for finite-size muon stoppers was performed "differentially" using the position information by the chamber in front of the polarimeter. From the measurements during 1996–2000, we accumulated 11.8×10^6 good events after the two-analysis combination, and deduced $P_T = -0.0017 \pm 0.0023(\text{stat}) \pm 0.0011(\text{syst})$, corresponding to the T-violating parameter $\text{Im}\xi = -0.0053 \pm 0.0071(\text{stat}) \pm 0.0036(\text{syst})$. From these results the upper limits of $|P_T| < 0.0050$ (90% C.L.) and $|\text{Im}\xi| < 0.016$ (90% C.L.) were deduced. Systematic errors were carefully studied and estimated. Almost all of the errors were canceled by the 12-sector summation and/or *fwd-bwd* subtraction, and the total systematic error was concluded to be as a half of the statistical error. The present result set constraints on model parameters of several theoretical models. For the three-Higgs-doublet model, e.g., a limit $|\text{Im}(\alpha_1 \gamma_1^*)| < 544(M_{H_1}/\text{GeV})^2$ was obtained. Implications for several other models are discussed.

PACS numbers: 11.30.Er, 12.60.Fr, 13.20.Eb

_____
*Second institutions are present addresses.
†Corresponding author.
Electronic address: jun.imazato@kek.jp
‡Deceased.

I. INTRODUCTION

Time reversal (T) symmetry has long been a subject of extensive interest in classical physics since it implies microscopic reversibility of motion. In quantum field theories, it has renewed aspects as a discrete symmetry along

with charge conjugation (*C*) and parity (*P*) [1]. The *CPT* theorem [2] asserts that a Lorentz-invariant field theory is unchanged under the combined *CPT* operation thus conserving *CPT*. Although *C* and *P* are each maximally violated in weak interactions, *CP* (and *T*) are nearly conserved. The violation of *T* has a great impact on our understanding of nature [3]. According to *CPT* invariance, however, the observation of *CP* violation in the K^0 [4] and B^0 [5] systems in 1964 and 2001, respectively, requires the existence of *T* violation.

A number of experiments to look for *T*-violating effects have been performed—reaction detailed balance tests [6], searches for *T*-odd correlations in decays in nuclear and particle systems [7], or searches for static electric dipole moments (EDM) [8]. However, a direct *T*-violation effect was not observed until 1998 when the CPLEAR experiment [9] found slightly different rates for $\bar{K}^0 \to K^0$ and its inverse $K^0 \to \bar{K}^0$ process in a Kabir test [10]. This discovery was followed in 1999 by the observation in the KTeV experiment of a large *CP*- and *T*-odd angular asymmetry [11] in $K_L^0 \to \pi^+\pi^- e^+e^-$ decays. These *T* asymmetries in the neutral kaon system could be accounted for consistently with the indirect *CP* violation in terms of ε although they were not unambiguous as direct tests of *T* violation [12].

In order to test the standard model (SM) and to search for physics beyond the SM, it is important to examine direct *CP* violation and also to perform searches for *T* violation in systems other than the neutral kaon. There are now several active fields of experimentation. The neutron EDM (d_n) is *P*- and *T*-odd. The upper limit has just been improved by a factor two to $3.1 \times 10^{-26} e$ cm [13] which is still several orders of magnitude above the SM prediction of $\sim 10^{-31}$ [8]. EDMs of other particles such as the electron [14] or atoms such as ^{199}Hg [15] also provide only upper bounds. Recent *T*-odd beta decay parameter measurements resulted in $D = [-2.8 \pm 6.4(\text{stat}) \pm 3.0(\text{syst})] \times 10^{-4}$ for the neutron decay [16], and $R = (0.9 \pm 2.2) \times 10^{-3}$ for the ^{8}Li decay [17]. Also, the recent measurement of transverse e^+ polarization with *T*-odd character in polarized μ^+ decay was consistent with no *T* violation ($P_{T_2} = (-3.7 \pm 7.7 \pm 3.4) \times 10^{-3}$) [18].

The *T*-violation effect in $K^+ \to \pi^0\mu^+\nu$ ($K_{\mu 3}^+$), the subject of the present paper, has several advantages for this purpose [19]. More than 50 years ago it was suggested by Sakurai [20] that the nonzero transverse polarization (P_T) of the muon in $K_{\mu 3}$ decay would be a definite signature of *T* violation. Here, one tests if the polarization of muons perpendicular to the kaon decay plane is nonzero. The unique feature here is the smallness of the final-state interactions which can mimic *T* violation by inducing a *T*-odd effect. That is the case for P_T in $K_L^0 \to \pi^-\mu^+\nu$ ($K_{\mu 3}^0$) or *T*-odd correlations in nuclear β-decays. Thus, P_T in $K_{\mu 3}^+$ can be regarded as an ideal system to look for *T* violation.

It has also been emphasized that a nonzero P_T is a sensitive probe of new physics because its SM contribution is small (10^{-7} [21]). Therefore, the present work can be regarded as a search for new physics. The SM cannot be an ultimate theory since it contains more than 20 arbitrary parameters and so it must be shaped by some new physics of higher rank. It has also been argued that the baryon asymmetry in the universe can be explained only with a new mechanism of *CP* violation [22]. In general, *T*- and *CP*-violation studies are considered to be among the most effective methods to search for new physics. Many efforts are also underway to find their evidence at collider machines. Decays such as $b \to s\gamma$ and semileptonic decay $B \to X\tau\nu$ are of this kind [23]. P_T, however, has competing or even higher ability to provide model constraints. Also P_T, as compared to the EDM experiments such as d_n, probes a different region of model parameter space. Thus, P_T is very complementary to other searches. It is noted that the effect of new interactions arises in P_T as an interference with the dominant SM process, thus appearing as proportional to the amplitude. P_T has also been studied in $K^+ \to \mu^+\nu\gamma$ [24] although the spurious effect from final-state interactions is larger there.

This paper is the final report of the KEK-E246 experiment which measured P_T in $K_{\mu 3}^+$ over 15 months during the period 1996–2000. The final result of the cumulative data was published in 2004 [25] as a letter and this paper presents all the details of this high-precision experiment to strengthen the reliability of the improved result. Section II is a brief review of the physics of transverse polarization in $K_{\mu 3}$ decay. The experimental method and apparatus are described briefly in Sec. III since the details have already been published elsewhere [26]. The data analysis of this experiment was carried out by two independent teams to minimize the individual biases. Details of analysis methods and policy are described in Sec. IV. The polarization analysis involving the determination of the analyzing power, and the calibration along with the results of P_T and Imξ are described in Sec. V. A precision measurement of this type is subject to various systematic errors, which require careful studies and these must be taken into account when quoting the final result. Section VI provides these details. Finally, Sec. VII is a brief discussion of the result and its implications for the models inspired by exotica such as multi-Higgs doublets or SUSY models. We also present a brief outlook for the future.

II. $K_{\mu 3}$ TRANSVERSE POLARIZATION

A. Phenomenology of $K_{\mu 3}^+$ decay

The matrix element for $K_{\mu 3}^+$ decay in the standard form of the V-A theory can be written as [27,28]

$$M \propto \frac{G_F}{2} \sin\theta_c [f_+(q^2)(p_K^\lambda + p_\pi^\lambda) + f_-(q^2)(p_K^\lambda - p_\pi^\lambda)]$$
$$\times [\bar{u}_\mu \gamma_\lambda (1 - \gamma_5) u_\nu], \tag{1}$$

with two form factors $f_+(q^2)$ and $f_-(q^2)$ of the momentum transfer squared to the lepton pair, $q^2 = (p_K - p_\pi)^2$. Here, G_F is the Fermi constant, θ_c the Cabibbo angle, p_K, p_π, p_μ, and p_ν are the four-momenta of the kaon, pion, muon, and antineutrino, respectively. Using $p_K = p_\pi + p_\mu + p_\nu$, Eq. (1) can be rewritten as

$$M \propto \frac{G_F}{2} \sin\theta_c [f_+(q^2)(p_K^\lambda + p_\pi^\lambda)\bar{u}_\mu \gamma_\lambda (1 - \gamma_5) u_\nu$$
$$+ f_-(q^2) m_\mu \bar{u}_\mu (1 - \gamma_5) u_\nu] \tag{2a}$$
$$= \frac{G_F}{2} \sin\theta_c f_+(q^2)[2p_K^\lambda \cdot \bar{u}_\mu \gamma_\lambda (1 - \gamma_5) u_\nu$$
$$+ (\xi(q^2) - 1) m_\mu \bar{u}_\mu (1 - \gamma_5) u_\nu]. \tag{2b}$$

The parameter $\xi(q^2)$ is defined as

$$\xi(q^2) = f_-(q^2)/f_+(q^2). \tag{3}$$

The first term of Eq. (2) corresponds to the vector (and axial vector) amplitude, and the second term corresponds to the scalar (and pseudoscalar) amplitude. Both f_+ and f_- can, in general, be complex, but if T invariance holds, then the parameter ξ should be a real number. Hence, any
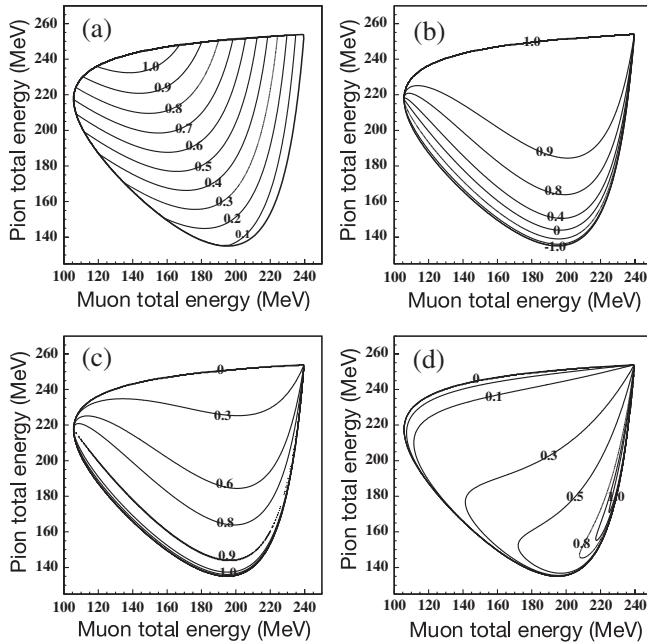

FIG. 1. The intensity distribution (a), and the three components of the muon polarization in the $K_{\mu3}$ decay of (b) longitudinal component P_L, (c) normal component P_N, and (d) transverse component $P_T/\text{Im}\xi$ as defined by Eq. (8). Here and in the Monte Carlo simulation later on, $\text{Re}\xi = -0.35$ was assumed, which was the evaluation value of the Particle Data Group at the start of the present experiment [29].

nonzero value of $\text{Im}\xi$ would imply T violation. The form factors f_- and f_+ depend on q^2 as

$$f_\pm(q^2) = f_\pm(0)[1 + \lambda_\pm(q/m_\pi)^2], \tag{4}$$

where the currently adopted values [28] of λ_+ and $\xi(0)$ are

$$\lambda_+ = 0.0284 \pm 0.0027 \tag{5a}$$
$$\xi(0) = -0.14 \pm 0.05 \tag{5b}$$

and $\lambda_- = 0$, namely, a constant f_-. The Dalitz distribution for $K_{\mu3}$ decay is given by [28]

$$\rho(E_\pi, E_\mu) \propto f_+^2(q^2)[A + B\xi(q^2) + C\xi^2(q^2)], \tag{6}$$

with

$$A = m_K(2E_\mu E_\nu - m_K E_\pi') + m_\mu^2(\tfrac{1}{4}E_\pi' - E_\nu) \tag{7a}$$
$$B = m_\mu^2(E_\nu - \tfrac{1}{2}E_\pi') \tag{7b}$$
$$C = \tfrac{1}{4}m_\mu^2 E_\pi' \tag{7c}$$
$$E_\pi' = (m_K^2 + m_\pi^2 - m_\mu^2)/(2m_K) - E_\pi. \tag{7d}$$

Here, E_π, E_μ, and E_ν are the pion, muon, and neutrino energies in the kaon center-of-mass frame, respectively, and m_K, m_π, and m_μ are the kaon, pion, and muon masses, respectively. The Dalitz distribution is shown in Fig. 1(a).

B. Transverse polarization P_T

One can define three orthogonal components of the muon polarization vector: the longitudinal (P_L), normal (P_N), and transverse (P_T) as the component parallel to the muon momentum $\vec{p}_\mu$, the component normal to P_L in the decay plane, and the component normal to the decay plane, respectively. They are expressed as

$$P_L = \frac{\vec{\sigma}_\mu \cdot \vec{p}_\mu}{|\vec{p}_\mu|} \tag{8a}$$

$$P_N = \frac{\vec{\sigma}_\mu \cdot (\vec{p}_\mu \times (\vec{p}_\pi \times \vec{p}_\mu))}{|\vec{p}_\mu \times (\vec{p}_\pi \times \vec{p}_\mu)|} \tag{8b}$$

$$P_T = \frac{\vec{\sigma}_\mu \cdot (\vec{p}_\pi \times \vec{p}_\mu)}{|\vec{p}_\pi \times \vec{p}_\mu|} \tag{8c}$$

with the polarization vector $\vec{\sigma}_\mu$. Using the decay probability Eq. (6) the muon polarization in the kaon rest frame can be written as [27,28]

$$\vec{\sigma}_\mu = \vec{A}/|\vec{A}|, \tag{9}$$

where $\vec{A}$ is determined as follows:

$$\vec{A} = \{a_1(\xi) - a_2(\xi)[(m_K - E_\pi)$$
$$+ (E_\mu - m_\mu)(\vec{p}_\pi \cdot \vec{p}_\mu)/|\vec{p}_\mu|^2]\}\vec{p}_\mu - a_2(\xi)m_\mu \vec{p}_\pi$$
$$+ m_K m_\mu \text{Im}(\xi)(\vec{p}_\pi \times \vec{p}_\mu). \tag{10}$$

Here,

$$a_1(\xi) = 2m_K^2[E_\nu + \mathrm{Re}(b(q^2))(E_\pi^* - E_\pi)] \quad (11a)$$

$$a_2(\xi) = m_K^2 + 2\,\mathrm{Re}(b(q^2))m_K E_\mu + |b(q^2)|^2 m_\mu^2 \quad (11b)$$

$$b(q^2) = \tfrac{1}{2}[\xi(q^2) - 1] \quad (11c)$$

$$E_\pi^* = (m_K^2 + m_\pi^2 - m_\mu^2)/(2m_K). \quad (11d)$$

These three polarization components are shown in Figs. 1(b)–1(d). One has to look for P_T in the presence of the predominant in-plane component with a size 1. P_T can be further written as an explicit product of $\mathrm{Im}\xi$ and a kinematical factor viz.,

$$P_T = \mathrm{Im}\xi \cdot \frac{m_\mu}{m_K} \frac{|\vec{p}_\mu|}{[E_\mu + |\vec{p}_\mu|\vec{n}_\mu \cdot \vec{n}_\nu - m_\mu^2/m_K]}. \quad (12)$$

Here, one clearly sees the advantage of $K_{\mu 3}$ over $K_{e3}(K^+ \to \pi^0 e^+ \nu)$ in the lepton mass dependence. Thus, P_T constrains $\mathrm{Im}\xi$. One may also discuss P_T in terms of coupling constants of exotic interactions in the generic effective four fermion Lagrangian [30,31]. An exotic scalar interaction is then responsible for $\mathrm{Im}\xi$, which can be written with Δ_S as

$$\mathrm{Im}\,\xi = \mathrm{Im}\Delta_S = \frac{(m_K^2 - m_\pi^2)\,\mathrm{Im}G_S^*}{\sqrt{2}(m_s - m_u)m_\mu G_F \sin\theta_C}, \quad (13)$$

where G_S is the scalar coupling constant, and m_s and m_u are the masses of the *s*-quark and *u*-quark, respectively. Thus, P_T constrains also G_S.

C. Model predictions and final-state interactions

A *T*-violating amplitude arises from the relative phases between diagrams or complex coupling constants in a diagram. Since only a single element of the Cabibbo-Kobayashi-Maskawa matrix V_{us} is involved for the *W*-exchanging semileptonic $K_{\mu 3}$ decay in the SM, no *CP* violation appears in the first order. The lowest order contribution comes from radiative corrections to the $\bar{u}\gamma_\mu(1 - \gamma_5)sW^\mu$ vertex (Fig. 2). This has been estimated to be less than 10^{-7} [21].

Spurious P_T^{em} can be induced by electromagnetic final-state interactions (FSI). Although it is much smaller than in
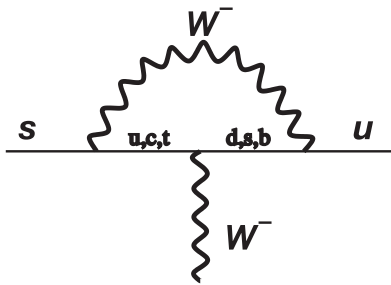

FIG. 2. Radiative corrections in the $K_{\mu 3}$ decay [21].

the case of P_T in $K_{\mu 3}^0$ decay, where the two charged particles can interact in the final state and $P_T^{em} \sim 10^{-3}$, this effect may limit the sensitivity for *T* violation and it has been extensively investigated. The single-photon contribution to P_T^{em} that arises in this decay due to the imaginary part of the two-loop diagram was estimated more than 20 years ago as $P_T^{em} \lesssim 10^{-6}$ [32]. Quite recently two-photon exchange contributions to P_T^{em} have also been studied in Ref. [33]. The average value of P_T^{em} over the Dalitz plot was concluded to be less than 10^{-5}. Thus, nonzero P_T in the range of $\sim 10^{-3}$–10^{-4} would unambiguously imply the existence of a new physics contribution.

The theoretical studies of P_T in various models of new physics have been of interest for many years and several calculations have been done. As candidate theories to give rise to sizable P_T, multi-Higgs models were studied [34]. In the 1990s, at the start of the present experiment there were renewed calculations in the framework of the three-Higgs-doublet model [35,36], leptoquark model [35,36], or some class of SUSY models [37,38] such as the *R*-parity breaking model, which all showed that P_T may be as large as 10^{-3} or even 10^{-2} without conflicting with other experimental constraints. On the other hand, in the framework of models such as minimal standard SUSY [37] or the left-right symmetric model [39], negligibly small P_T is given. Clearly, an improvement in the measurement of P_T will constitute an important tool to constrain these different models. In the three-Higgs-doublet model the importance of a P_T measurement in $K^+ \to \mu^+\nu\gamma$ as well as in $K_{\mu 3}$ has been pointed out [31].

D. Previous studies of P_T in $K_{\mu 3}$

Early experimental measurements of P_T were carried out at the Bevatron [40] and Argonne [41] in $K_{\mu 3}^0$ decays but with less statistical significance. The final-state interactions also obscure the real P_T. More advanced experiments prior to our work were carried out at the 28 GeV AGS machine at the Brookhaven National Laboratory (BNL), where Morse *et al.* [42] measured the P_T of muons from in-flight $K_{\mu 3}^0$ decays. From a data sample of 12×10^6 events, they deduced $\mathrm{Im}\xi = 0.009 \pm 0.030$. This result, while consistent with zero, has a central value compatible with a prediction of 0.008, from the *T* invariant final-state interactions. At the same facility, Blatt *et al.* [19] measured P_T of $K_{\mu 3}^+$ for the first time by detecting neutral particles

TABLE I. Previous experiments and their $\mathrm{Im}\xi$ results.

Laboratory	Decay	Year	$\mathrm{Im}\xi$	Ref.
Bevatron	$K_{\mu 3}^0$	1967	-0.02 ± 0.08	[40]
Argonne	$K_{\mu 3}^0$	1973	-0.085 ± 0.064	[41]
BNL-AGS	$K_{\mu 3}^0$	1980	0.009 ± 0.030	[42]
BNL-AGS	$K_{\mu 3}^+$	1983	-0.016 ± 0.025	[19]

from the in-flight decay of an unseparated 4 GeV/c K^+ beam. From a data sample of 21×10^6 events, they deduced Im$\xi = -0.016 \pm 0.025$, consistent with T invariance. These results are summarized in Table I.

III. EXPERIMENT

A. Overview of the apparatus

The present experiment was performed using a toroidal spectrometer setup in conjunction with a stopped K^+ beam at the low momentum separated kaon beam line K5 in the North Experimental Hall of the KEK 12-GeV proton synchrotron. The spectrometer comprised an iron-core superconducting toroidal magnet with 12 gaps [43]. The setup is shown in Fig. 3. The K^+ were stopped in an active target located at the center of the magnet. $K_{\mu3}$ decays were identified by detecting a π^0 with a CsI(Tl) barrel surrounding the target, a muon with a charged particle tracking system consisting of chambers, C2, C3, and C4, and the target and ring fibers (target/ring) together with particle identification by means of time-of-flight (TOF). This arrangement enabled a measurement of the decay pions ranging over all directions covering all regions of the decay phase space for a given μ^+ momentum. As described next, this scheme allowed a "double ratio" measurement and, thus, a number of systematic errors could be suppressed.

The CsI(Tl) barrel had 12 holes to admit charged particles into the magnet gaps. Since the barrel does not cover the full 4π solid angle, not all events had the two photons from π^0 decay detected. However, one photon with relatively large energy could also be used to determine the π^0 momentum. Muons were bent by about 90 deg, momentum analyzed, and then they entered the muon polarimeter.

After passing through a polarimeter trigger counter, and being momentum-degraded by a wedge-shaped Cu plate, the muons were stopped in an array of pure Al plates.

The muon polarization was measured by means of the decay positron asymmetry. When π^0s are detected in the forward (*fwd*) or backward (*bwd*) directions relative to the beam axis, the transverse component P_T lies in the azimuthal directions in each stopper clockwise (*cw*) or counterclockwise (*ccw*), respectively, as an azimuthal polarization (Fig. 4). Thus, the magnitude of the transverse polarization $P_T \sim \vec{\sigma}_\mu \cdot \vec{p}_{\pi^0} \times \vec{p}_{\mu^+}$ can be measured as the azimuthal asymmetry of positron emission, namely, a *cw* and *ccw* emission rate difference.

B. Stopped beam method

A distinct feature of the present experiment was the adoption of the stopped beam method in contrast to the previous BNL experiments. There are several advantages to the stopped beam in the present high-precision experiment, although with low-momentum beams the number of stopped kaons is, in general, lower. The conceptual merits of the present setup can be summarized as follows.

(a) Full kinematic determination with high resolution.— When both photons from π^0 decay are measured allowing a reconstruction of the π^0, the measurement of the μ^+ together with the confirmation of the kaon stopping position completes the decay kinematics with $\vec{p}_{K^+}$, $\vec{p}_{\pi^0}$, and $\vec{p}_{\mu^+}$, which can be checked with the missing mass corresponding to the neutrino mass. The low photon energy and muon momentum in the kaon center-of-mass system have shorter ranges and thus are easily detected and analyzed. The high angular resolution over 4π directions assures high decay kinematic resolution, thus the photon calorimetry becomes very relevant in the final resolution.
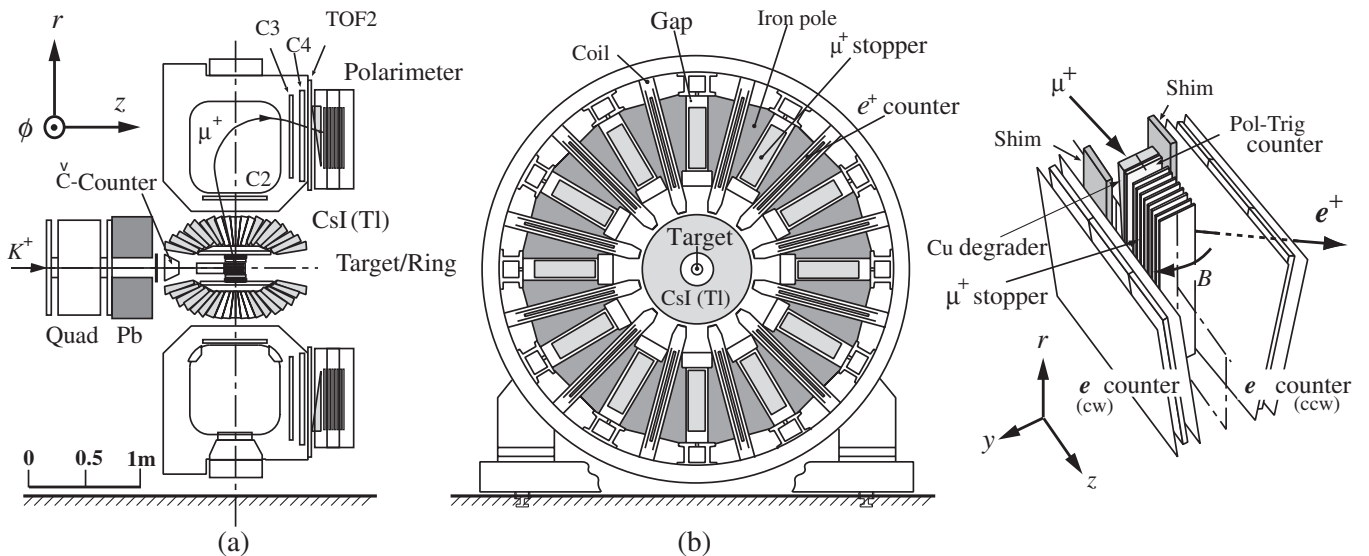

FIG. 3.   Experimental setup: (a) cross section side view, (b) end view, and (c) schematic view of one sector of the polarimeter. For details see [26].
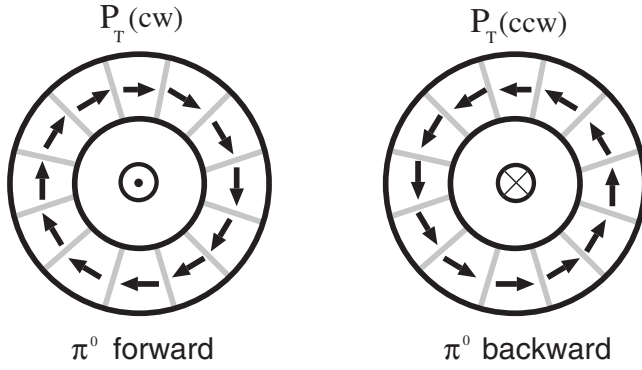
FIG. 4. T-violating azimuthal polarization P_T for the cases of the π^0 going in the forward (*fwd*) and backward (*bwd*) directions.

(b) Total coverage of decay kinematics.—The π^0 detector covers all directions. Although there is a window for the muon momentum $\vec{p}_{\mu^+}$, all $\vec{p}_{\pi^0}$ are detected for a given $\vec{p}_{\mu^+}$. Thus, the polarization is measured for $-\vec{p}_{\pi^0}$ as well as for $\vec{p}_{\pi^0}$ for which

$$P_T(-\vec{p}_{\pi^0}) = -P_T(\vec{p}_{\pi^0}) \tag{14a}$$

$$P_N(-\vec{p}_{\pi^0}) = -P_N(\vec{p}_{\pi^0}) \tag{14b}$$

hold. This feature enables an experiment with a double ratio technique by comparing the polarization for $\vec{p}_{\pi^0}$ and $-\vec{p}_{\pi^0}$. In the present experiment, the azimuthal polarizations when the π^0 are going in the forward direction (P_T^{fwd}) and in the backward direction (P_T^{bwd}) were measured with the expected relation of

$$P_T^{fwd} = -P_T^{bwd} \tag{15}$$

as shown in Fig. 4 and we could double the effect by taking their difference, $2P_T = P_T^{fwd} - P_T^{bwd}$. The absence of biases in the polarimeter defined as the "null asymmetry A_0" can be checked by observing the azimuthal asymmetry (perpendicular to the muon momentum, p_{μ^+}) of all the events with p_{π^0} and $-p_{\pi^0}$ since $P_T(\vec{p}_{\pi^0}) + P_T(-\vec{p}_{\pi^0}) = 0$ and $P_N(\vec{p}_{\pi^0}) + P_N(-\vec{p}_{\pi^0}) = 0$.

(c) No effects of beam emittance.—By stopping the beam one can decouple the experiment from the beam emittance except for the stopping distribution. Once the beam is stopped, one can forget about the incident beam angle, which might produce a screw-sense spurious effect when coupled with another displacement vector, and can start from the stopping distribution. Its asymmetry, if any, can easily be taken into account and corrected.

(d) Lower backgrounds.—First, the full kinematical measurement and relatively low momentum of decay particles in the kaon center-of-mass system enables the $K_{\mu 3}$ event identification with only a small contamination from physics backgrounds. Second, in the E246 setup, all the detector elements except for the beam counters and the target are located off axis. Thus, they do not suffer from

high counting rates. Only the inner part of the CsI(Tl) suffered from hits by the beam halo. The great advantage was the location of polarimeter which is far outside of the beam axis and behind the spectrometer magnet. This provided an ideal environment with very low background for the muon decay positron measurement. This feature is in distinct contrast to the previous BNL in-flight-decay experiment where the polarimeter was located in the beam region.

(e) Relatively small setup.—The setup of E246 is practically a single structural unit with a relatively short length. Hence, the alignment of each detector element, which is one of the essential requirements for a high-precision experiment, is not very difficult. The control of systematics is also easier for a short apparatus.

C. Longitudinal field asymmetry measurement

1. Longitudinal field method

In the present work, the longitudinal field method was adopted. Namely, the field was parallel to the relevant polarization component, P_T, and perpendicular to the other in-plane components, The asymmetry is an observable defined as

$$A = \frac{N_{cw} - N_{ccw}}{N_{cw} + N_{ccw}} \tag{16}$$

with the *cw* and *ccw* counts N_{cw} and N_{ccw}, respectively. A measurement to determine the $A_0 = 0$ line by some means becomes essential.

A magnetic field was guided onto the muon stoppers using well-aligned iron shim plates. Although the field flux was curving at the stopper, it provided a longitudinal configuration on average. The azimuthal polarization; namely, the transverse polarization in the case of *fwd* and *bwd* pions, is preserved while the radial and axial components from the T-conserving in-plane components precess around the field. The application of a longitudinal field will decouple the spins from all the small stray fields at the setup including the earth's field. On the contrary, the alignment of the field becomes very important thus defining the reference axis for the polarization. There is no necessity to reverse the field since the asymmetry baseline, A_0, can in principle be canceled out by taking the difference between *fwd* and *bwd*.

2. Preservation of transverse polarization

In the polarization measurement it is a prerequisite that there is no perturbation of the polarization until the moment of the muon decay.

(a) Muon spin depolarization in flight.—There are no magnetic materials in the path except for the iron cores of the magnet. The surface of the pole face is magnetized azimuthally, and a scattered muon can pick up azimuthal polarization from the electron spins. However, this effect

was estimated to be negligibly small and the analysis could also cut such scattered events. Furthermore, this effect is common to *fwd* and *bwd*. The second effect to be checked is the depolarization due to multiple scattering in the Cu degrader and the Al stopper, which is significant. However, the depolarization is essentially a relativistic effect and thus not predominant for slow muons. The depolarization for the transverse component was calculated according to [44] to be small enough in the present case.

(b) Depolarization after stopping.—It is known that there is no formation of muonium leading to the loss of the initial polarization after stopping in pure Al metal [45]. It is also known that there is no significant spin relaxation in Al (without magnetic impurities [46] or dislocations) at room temperature. These conditions were further ensured with an application of an external field. Very pure Al metal plates with purity higher than 99.999% were used as the stopper material. Thus, there was no reason for any depolarization before the decay. The relaxation time of the polarization in the actual material was measured to be longer than 20 μs in a transverse-field precession measurement carried out at a muon beam line at the Meson Science Laboratory [47] by applying an external field of 1 kG.

D. Apparatus and its performance

1. Kaon beam and target

A K^+ beam was extracted at the K5 low-momentum kaon line [48] with a typical intensity of 3×10^5 kaons per spill. A spill duration of 0.7 s and repetition rate of 2.7 s were selected so as to attain the highest sensitivity for the experiment taking into account the accidental pileup effect in the CsI(Tl) detector. A K^+ beam momentum of 660 MeV/c was adopted to maximize the stopping rate in the target. A π^+ to K^+ ratio of typically 8 was obtained. The beam was accompanied by a pion halo; this was the main source of accidental hits on the CsI(Tl) crystals.

The beam, collimated by a heavy metal collimator system at the exit of the channel, was counted by a beam hodoscope B0, and entered the Fitch-type beam Cherenkov counter [49] system, whose details are described in [26]. The passage of a K^+ generated a light cone which was counted by a ring of photomultiplier tubes (PMTs) giving a signal for a K^+. On the other hand, the passage of a π^+ generated a different light cone. Figure 5 shows the multiplicity spectrum of both rings for incident K^+ and π^+ beams.

The beam momentum was then lowered by a degrader system with 6.5 cm of Al metal followed by 24.2 cm of BeO and stopped in a target consisting of 256 scintillating fibers with 5×5 mm^2 cross section. The thickness of the degrader was adjusted so that the K^+ stopping distribution was centered in the 20 cm long fiducial region of the target. A kaon hit was identified by the fiber with the largest

energy deposit. The stopping efficiency determined as the ratio to the Cherenkov counter incoming beam was 39%. Figure 6 shows the stopping distribution of relevant $K_{\mu3}$ kaons. Since the beam had non-negligible dispersion at the final focus there was a tilt in the horizontal projection of the stopping distribution.

2. Spectrometer and charged particle tracking

The superconducting toroidal spectrometer [43] consisted of 12 identical sectors, each having an iron yoke and a parallel gap of 20 cm. The maximum design field in the gap was 1.8 T, but only 0.9 T was used in the present experiment to obtain the optimum acceptance for $K_{\mu3}$ muons in the polarimeter. The magnet was manufactured with high precision to obtain good 12-fold rotational symmetry. The 12 median planes of the gaps crossed each other within 2 mm of the hypothetical beam axis. The field distribution was mapped with a three-dimensional field calculation code TOSCA [50] inputting realistic magnetic parameters of core iron and geometry. The magnet was excited for each beam cycle of typically several weeks. Although no hysteresis was observed, the excitation cycling between 0 and 0.9 T was strictly kept all through the experimental period of 5 years. In order to avoid any effects related to temperature, the spectrometer was sitting in an air-conditioned room and the ambient temperature was kept constant ($T = 20.0 \pm 0.5 °C$).

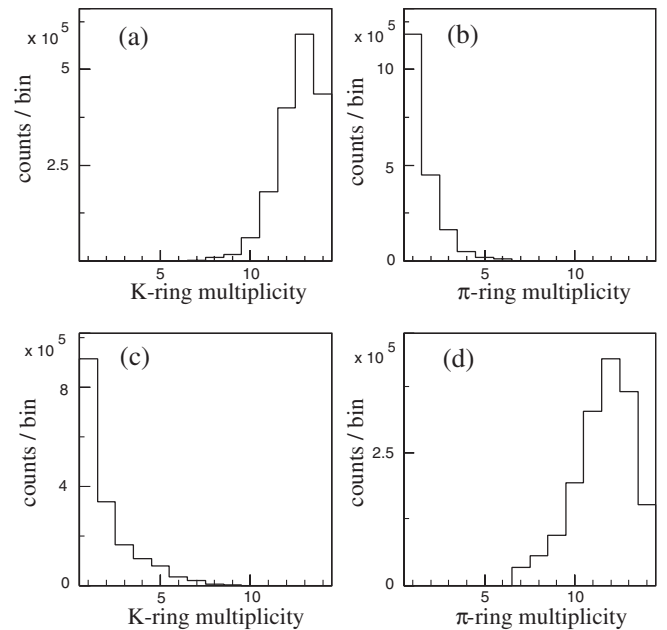For the tracking elements we used C2, C3, and C4 multiwire proportional chambers (MWPC) and an active

FIG. 5. Beam Cherenkov counter multiplicity spectrum: (a) kaon ring spectrum at kaon incident, (b) pion ring at kaon incident, (c) kaon ring at pion incident, and (d) pion ring at pion incident.
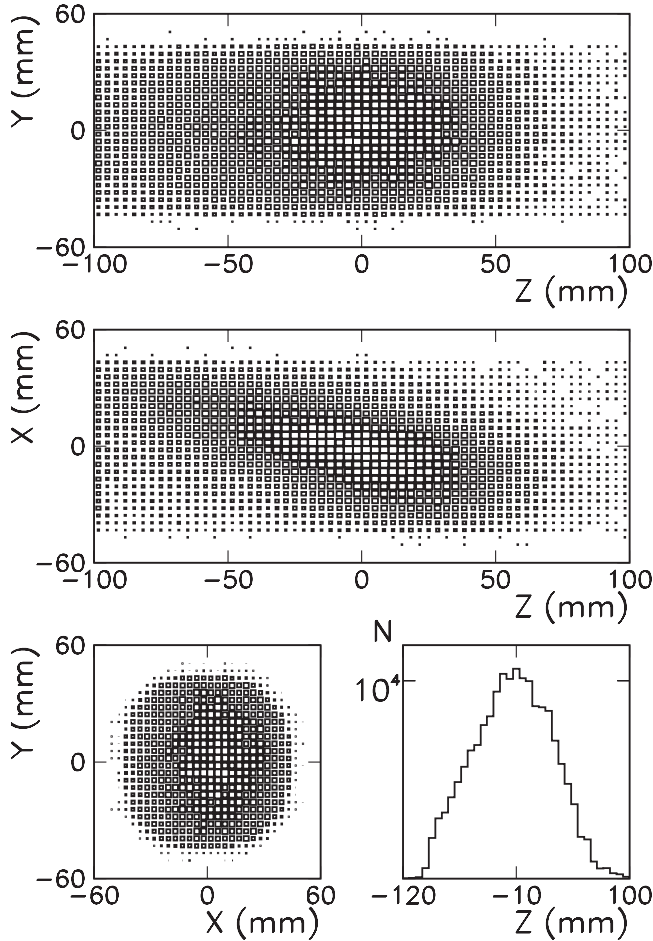
FIG. 6. Kaon stopping distribution in the target: $\rho(y, z)$ (up), $\rho(x, z)$ (middle), $\rho(x, y)$ (lower left), and the z projection (lower right) in the target with an array diameter of 93 mm and a fiducial z length of 20 cm.

target and ring (target/ring) system [51]. The target/ring was added to the tracking program although its size was 5 mm square for the target giving x and y information and 6 mm wide for the rings which provided z information. The typical position resolution of the chambers in cathode readout (z coordinate for C2 and r coordinate for C3 and C4) was about 80 μm, with some degradation for oblique incidence. The orthogonal directions had only the resolution of the anode wire spacing (2 mm). The charged particles were triggered by 12 target fiducial (Fid) counters with a 20 cm long sensitive region surrounding the target centered at $z = 0$. These signals were used as the time origin of the master trigger signal as well as the start signal for the TOF measurement.

The stop signal of the TOF was provided by a 2 cm thick counter TOF2 located at the exit of each gap. The bent particles were momentum degraded by a wedge-shaped Cu degrader to equalize the stopping depth of the muons at the gap exit and entered the polarimeter after hitting the polarimeter trigger (Pol-trig) counter just behind the degrader.

The muon stopper was located roughly at the quasifocal plane of the 90 degree sector dipole, thus providing a high collection efficiency for the muons.

3. π^0 detection

The electromagnetic calorimeter [52] to detect the π^0s was a barrel structure surrounding the target with "muon holes" at $\theta = 90°$ to allow the charged particles to enter the 12 spectrometer gaps. The barrel consisted of 768 CsI(Tl) crystals, each pointing to the center of the target with segmentation angles (polar as well as azimuthal) of $\Delta\theta = \Delta\phi = 7.5°$ with the exception of the innermost layer close to the beam axis which had $\Delta\phi = 15°$, and for the parts in between the muon holes. There were also beam entrance and exit holes; thus the solid angle coverage was only about 75%. All the crystals had a length of 25 cm corresponding to a radiation length of $13.5X_0$. The barrel was carefully assembled with a precision of about 1 mm in order to assure rotational as well as fwd/bwd symmetry.

Because the outer region of the calorimeter was under a fairly strong stray magnetic field of the spectrometer and also because the space was very tight, PIN photodiode readout (which is insensitive to magnetic fields) was employed. A large size diode (18×18 mm or 28×28 mm) was glued on the rear surface of the crystal and a high light yield of 11 000 photoelectrons/MeV (for 18×18 mm PINs) was obtained enabling us to lower the photon detection threshold. The noise level after a charge-sensitive amplifier was 65 keV in equivalent noise level. Details of the CsI(Tl) electronics can be found elsewhere [53].

The signal from the preamplifier was fed to an amplifier which generated two output pulses: one was a shaped slow pulse to a peak-hold analog-to-digital converter (ADC) for an energy measurement, and the other was a timing filter amplifier pulse for a timing measurement and the logic circuits. The average time resolution of the crystals was $\sigma_t = 3$ ns at the energy deposit of 100 MeV with decreasing (increasing) values for higher (lower) energies.

All the crystals were calibrated with $K_{\mu2}$ muons with an energy deposit of 152 MeV and with the sum energy of two photons from π^0 of $K^+ \rightarrow \pi^+ \pi^0$ ($K_{\pi2}$) with 245 MeV. The calibration was extrapolated by means of a Xe-lamp light signal fed to each crystal by a fiber. The invariant mass of two photons from π^0 decay of $K_{\pi2}$ shows a tail on the lower mass side due to lateral leakage of the shower (mainly into the muon holes) and the main Gaussian part is consistent with what is expected from the energy resolution of each crystal, $\sigma_E/E = 3\%$ at 1 GeV, which was measured in an independent test measurement. A typical $K_{\mu3}$ event has a cluster size of 3×3 crystals and the cluster timing resolution of $\sigma_t = 3$ ns. The angular resolution could be inferred from the $\pi^+ \pi^0$ angle correlation in $K_{\pi2}$ since the direction of the π^+ was determined very accurately by the MWPCs.

The counting-rate performance was limited by the width of the shaping-amplifier output pulse with a 1.0 μs shaping

time as well as the dynamic range of the preamplifier output. Both allowed rates of $10^4/s$ with a small pileup or loss rate of 5%. The shaper output was fed to a transient-digitizer (TD) system in preparation for the use in the case of high pileup rate. However, this was not necessary in the actual analysis.

4. Muon polarimeter

After passing the Pol-trig counter located behind the Cu degrader, the muons were stopped in an array of 8 Al plates of 6 mm thickness with size of 16 cm width and 55 cm height with 8 mm spacing in between. The width was smaller than the spectrometer gap of 20 cm and the Pol-trig counter width of 18 cm so that all the stopped muons would generate a trigger. The height was chosen to cover the necessary momentum range and the total Al thickness of 48 mm was enough to stop muons in a wide momentum range with an efficiency of more than 85%. The spacing lowered the effective average density of Al to suppress the e^+ interaction creating nearly optimum conditions for the asymmetry measurement. Veto-counters behind the stopper detected nonstopped muons to suppress background decays from the surroundings.

The holding field strength applied by two iron shim plates aside the stopper varied from 300 to 150 G (Fig. 7) with a vector direction as shown. The shim plates were aligned with a precision better than 200 μm relative to the magnet gap so as to produce a symmetric field distribution across the median plane. A field mapping was performed to check the field symmetry and to measure its strength distribution for all 12 gaps. The apparatus and method used has been described in detail elsewhere [54]. By means of the novel method of four settings of the Hall-element angle, the field vector could be analyzed with a precision of 1 mr.

Positrons were counted by a plastic counter (e^+ counter) of 6 mm thickness segmented in three parts in coincidence with two sandwich coincidence counters of 3 mm thickness. The counter system was aligned with a precision of a few mm relative to *cw* as well as *ccw* stoppers. One positron counter system served as both the *cw* and *ccw* counter with the same detection efficiency. The solid angle of detection (about 10% on each side) was determined by the three e^+ counters and the detection threshold was set at 5 MeV. The positron time spectra were measured with a multistop time-to-digital converter (TDC) with a time range of 20 μs relative to the time origin of the TOF2 counter.

5. Trigger and data acquisition

In the normal runs the trigger condition for data acquisition was the mixture of the standard trigger T_{std} for the main data taking and a prescaled T_{pre} for an open condition. T_{std} was the multiple conditions of
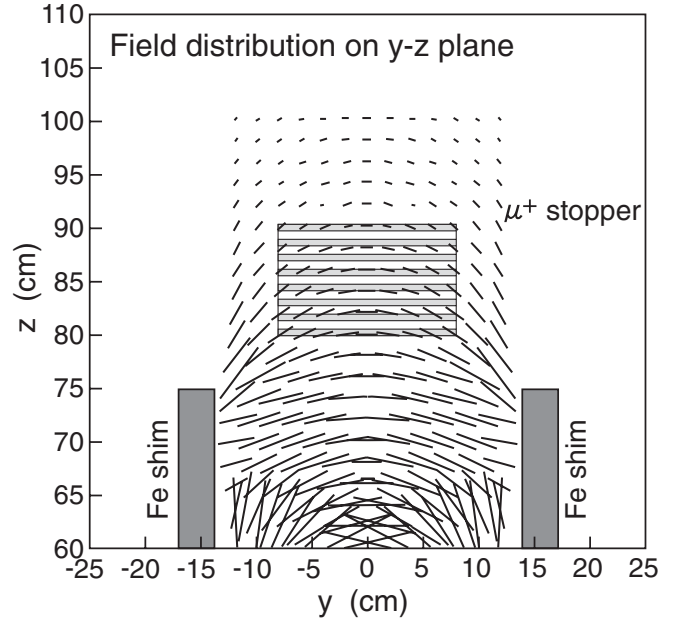

FIG. 7. Muon stopper configuration and magnetic field distribution. The direction of the flux is only schematically illustrated.

$$T_{std} = C_K \cdot \text{Fid} \cdot \gamma \cdot \text{TOF2} \cdot \text{Pol} \cdot e^+, \qquad (17)$$

where (i) C_K is the kaon incident signal defined as the Cherenkov counter kaon ring multiplicity larger than 6 ($N_K \geq 7$), (ii) Fid is the hit of one of the Fid counters to identify a decay associated with charged particle emission, (iii) γ is the firing of at least one CsI(Tl) crystal with more than 10-MeV energy deposit assuring the detection of at least one photon, (iv) TOF2 is the firing of the TOF stop counter, (v) Pol is the firing of the Pol-trig ensuring the entry of a muon into the polarimeter, and (vi) e^+ is the detection of a positron in either the *cw* or the *ccw* positron counter. This condition was checked for each gap and an OR of the 12 gaps was used as the trigger. In order to investigate the background conditions, the trigger signal T_{pre}, with no γ requirement in the standard trigger, was admixed after prescaling by a factor of 30. A typical trigger rate was 100/spill and ADC and TDC as well as other data such as scalers were read out. These data were read mainly by TKO (the KEK standard crate system [55]) and FASTBUS via Versa Module Eurocard (VME) to a board computer (HP-753) by means of the data taking program UNIDAQ [56]. Details are described in [26]. The typical dead-time was 10%–15%.

6. Total performance of the detector

The charged particle acceptance was determined mainly by the aperture of the toroidal spectrometer. The necessary size of the muon holes was optimized to achieve the maximum acceptance for $K_{\mu 3}$ events when two γs were detected. The energy dependence of the γ acceptance is flat, and the same is true for the π^0 energy dependence.
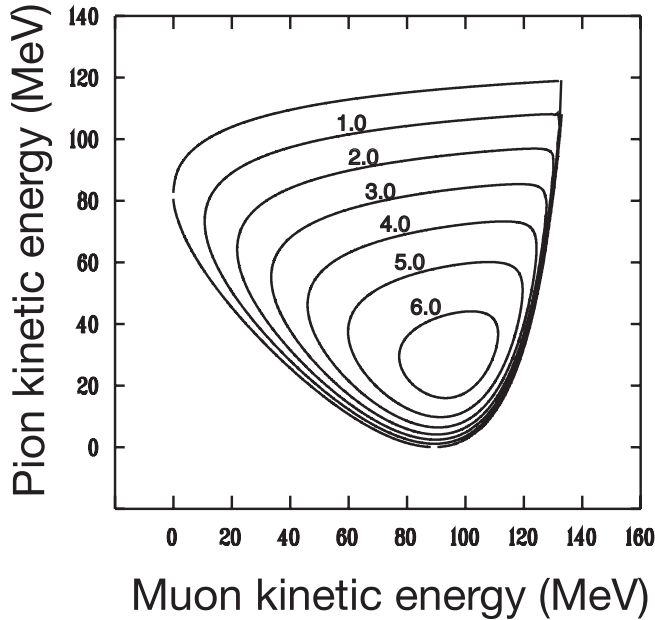
FIG. 8. Figure-of-Merit (FoM) distribution of P_T measurement on the Dalitz plane. The FoM is defined as $P_T \times \sqrt{N}$. The contour is the linear step from 0 to 6.

Thus, it was only necessary to adjust the spectrometer momentum range in order to obtain the highest sensitivity to P_T. The present spectrometer did not have full range coverage. The region of 100 to 190 MeV/c was selected as the central momentum range to cover the figure-of-merit peak in the Dalitz plot (Fig. 8). The detector acceptance for 2γ and 1γ events are shown in Fig. 9. The geometrical acceptance of the detector was estimated to be $\sim 10^{-4}$ including the small solid angle for positron detection.

7. Data taking

Data taking was conducted during the years 1996–2000 as three blocks of runs each lasting several weeks. This beam time schedule was mandated by the general experimental coordination of the KEK 12-GeV proton accelerator. The beam conditions were slightly different each time and the intensity was maximized (within the acceptable
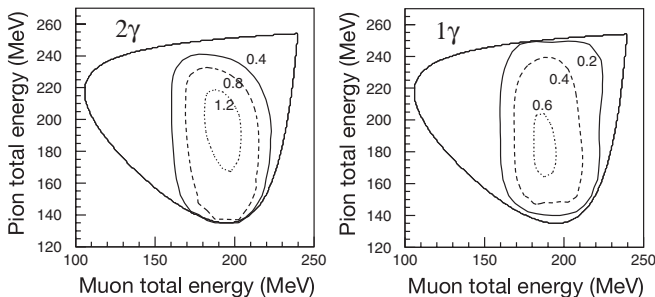

FIG. 9. Detector acceptance for 2γ events (left) and 1γ events (right) of the detector on the Dalitz plane. The height of the contour is in relative scale.

TABLE II. Beam cycle summary.

Data period	I	II	III
Year	1996, 1997	1998	1999, 2000
Data taking hours	1590	1810	1740
Typical p intensity[a]	$0.9 \times 10^{12}/s$	$1.0 \times 10^{12}/s$	$1.1 \times 10^{12}/s$
Typical K^+ intensity[a]	$1.0 \times 10^5/s$	$1.2 \times 10^5/s$	$1.3 \times 10^5/s$

[a]Average intensity during the beam spill period of 2.7 s.

pileup range) by adjusting the slit aperture of the secondary line. Accordingly, the trigger rate was slightly changed and the background conditions in the CsI(Tl), in particular, were different every time. The main parameters of the beam cycles are summarized in Table II.

IV. DATA ANALYSIS

The analysis was performed independently by two analysis teams (A1 and A2) following their own analysis philosophies. This two-analysis method provided not only the means to cross-check the final results but also to estimate the systematic error associated with the analysis. It also enabled data quality checks in each analysis by sorting events into the categories (common or uncommon) to the selected events in the other analysis. This type of global data quality check would have been impossible if only a single analysis had been performed unless one investigated all kinds of dependence of P_T on variables thoroughly. However, it is very impractical from the statistical significance point of view. The results from both analyses were then combined in a statistically appropriate way with an increased number of events compared to the individual analyses as a by-product. This method also enabled us to find potential errors in the data handling and processing in the analysis stage.

The analysis was processed for the three data periods of I, II, and III separately to examine the time dependence and data dependence, if any. The grouping of runs into these three data sets was arbitrary but the selection was such that each data set consisted of measurement runs with nearly the same beam condition and nearly the same number of events. For the 1996–1997 data the result was published in 1999 [57]. The analysis code (event selection method) was slightly improved for the analysis of the 1998–2000 data sets. In [57] the polarimeter analysis was performed by using the *cw* and *ccw* respective total counts (the integral method); however, the data were processed below by means of the differential method (see later) together with the 1996–1997 data and this result was reported in [25] and is presented in this final paper.

Analysis was done in the scheme of:
(1) $K_{\mu3}$ event selection in two individual analyses,
(2) Data quality checks for the selected events,
(3) Combination of the two analyses,
(4) Data quality checks for the combined data sets,

(5) Extraction of P_T in the polarimeter analysis.
In the following, we first describe the procedures which were common to both analyses and the details of the data quality check method. Then, different features of each analysis are presented, followed by "the combination." The description of the polarimeter analysis and its result are shown in the next section.

A. Common procedure

1. Event selection

The data obtained under the standard trigger condition were processed. The concept and basic parts of $K_{\mu3}$ event selection were very similar in both analyses, removing unnecessary $K_{\pi2}$ and K_{e3} events in the triggered data. A $K_{\mu3}$ event was identified uniquely by detecting a μ^+ and a π^0 in the relevant energy regions following a kaon stop. The condition of a kaon stopping in the target was confirmed by taking the delayed part of the timing between the kaon hit in the beam Cherenkov counter or the target fiber and the decay particle hit in the Fid counter (Fig. 10). There is a small fraction of kaons emerging from the momentum degrader which decay in flight before stopping. Such in-flight events, having not only p_z but also p_x and p_y, resulted in a rotation of the decay plane from that of at-rest decays, and had to be rejected. This could be achieved by cutting the prompt peak in the kaon decay time spectrum.

For the muon analysis, a hit in the Fid, TOF2 and Pol-trig counters in the trigger assured a charged particle. By using the information of chambers C2, C3, and C4 and the target/ring scintillator, a track was reconstructed and its

FIG. 11. A typical charged particle momentum spectrum of all the 2γ and 1γ events. The bump below 190 MeV/c containing $K_{\mu3}$ and K_{e3} was accepted in the analyses.

momentum (p) was determined from the field map. Since the charged particle passed through thick target material an energy loss correction was essential to determine its true energy. This correction was done using the target decay vertex point and the energy deposit signals in the penetrated fibers. Although there were substantial differences in the track reconstruction codes of A1 and A2, the obtained
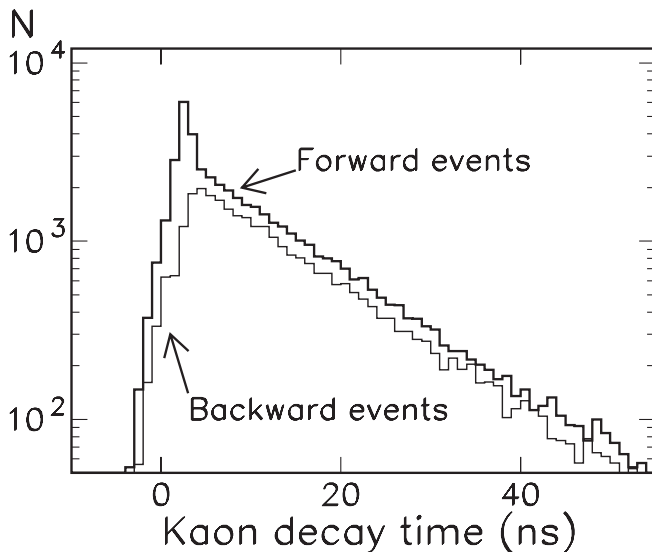

FIG. 10. Kaon decay time distribution measured as a difference between the target fibers timing and the Fid-counter decay particle timing for the total events of 2γ and 1γ. In the forward π^0 spectrum, one sees a peak at the prompt timing coming from K^+ decay-in-flight which was removed in the analysis.
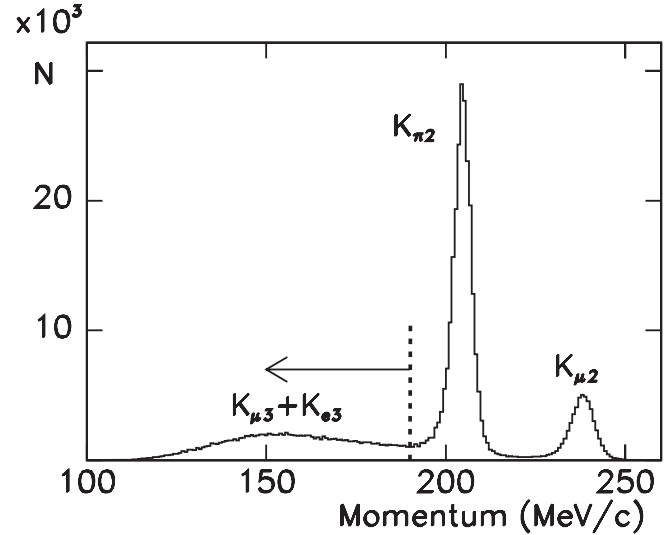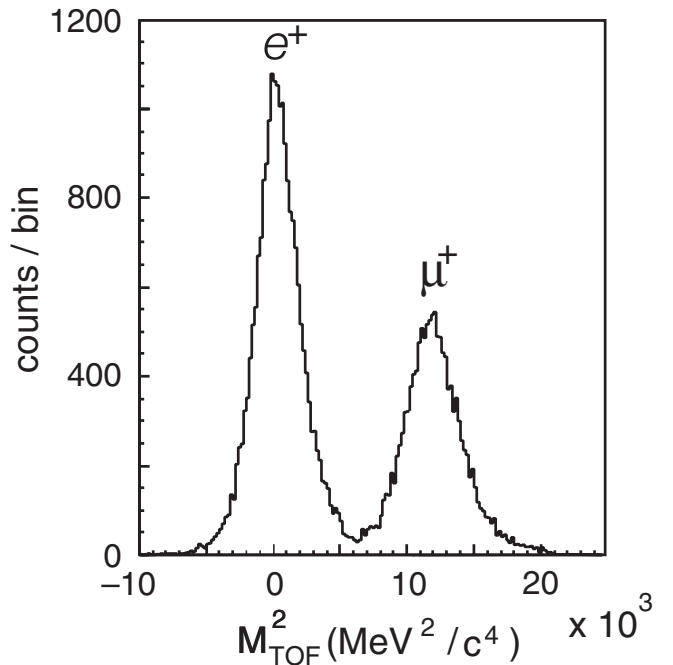

FIG. 12. TOF mass spectrum of charged particles in the momentum range of 100 to 190 MeV/c in the analysis A1. The positrons from K_{e3} could be rejected.

momentum spectra were very similar and the predominant background mode of $K_{\pi 2}$ could be primarily rejected (see Fig. 11). The bump at $p = 100 \sim 190$ MeV/c, however, consists not only of $K_{\mu 3}^+$ muons but also of K_{e3}^+ positrons. The time-of-flight measurement was very effective to remove this K_{e3}^+ background (Fig. 12). The stopping distribution of muons triggered by e^+ detection along the y direction as measured by the C4 chamber is shown in Fig. 13. The mass of charged particles was calculated as

$$M_{\mathrm{TOF}}^2 = \frac{p^2}{c^2}(1/\beta^2 - 1) \tag{18a}$$

$$\beta = \frac{L_f}{\Delta t \times c}, \tag{18b}$$

where L_f and p are the path length between the two counters and the momentum calculated by the tracking analysis and Δt is the time of flight.

Since the CsI(Tl) detector had only 3/4 of the full solid angle coverage, the events in which both the π^0 decay
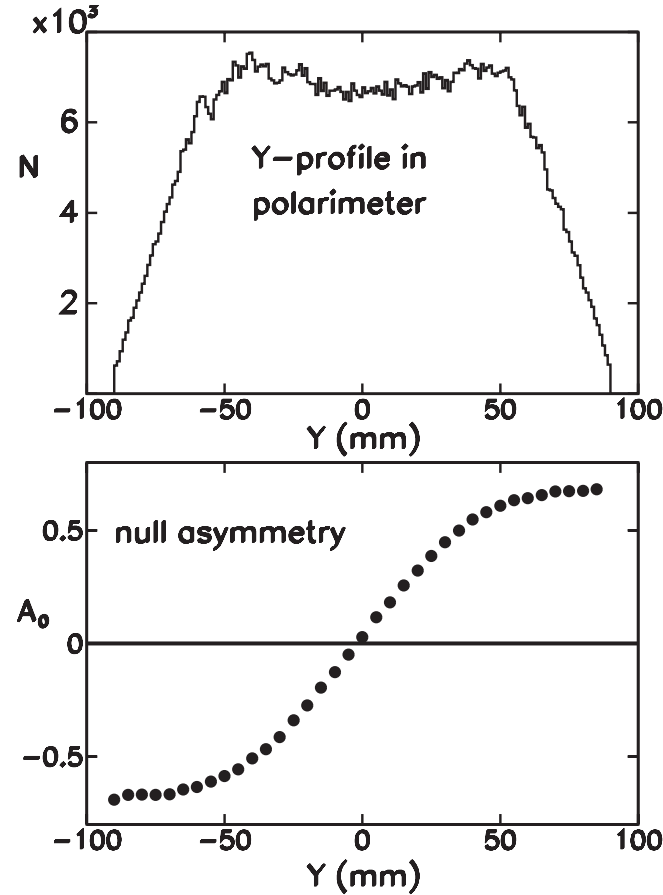

FIG. 13. Incident muon y distribution in the stopper measured by the C4 chamber (top), and the intrinsic geometrical asymmetry for those muons (bottom). The real stopping distribution has a smearing due to beam divergence and multiple scattering. The geometrical asymmetry was measured as the null asymmetry A_0 by accepting all π^0 directions.

photons were detected (2γ events) and those in which a single photon was detected (1γ events) were included in the analysis. In the case of 2γ the reconstruction of the decay kinematics was exact. However, for 1γ events, one had to select events with higher photon energy to obtain better kinematical reconstruction. The ambiguity of the initial π^0 direction degraded the sensitivity to P_T through the smearing of the decay plane. The energy threshold was determined so as to obtain the maximum sensitivity of $\sqrt{N_\gamma}\langle\cos\phi_\gamma\rangle$. Here, N_γ is the photon yield and $\langle\cos\phi_\gamma\rangle$ is the average of the cosine of the photon angle relative to the initial π^0 direction. This figure of merit was studied by a Monte Carlo simulation with realistic detector response in each analysis and an optimum threshold energy of $E_\gamma^{\min} = 70$ MeV was adopted common to both. The average attenuation factor was $\langle\cos\phi_\gamma\rangle = 0.70$. The fraction of one photon events in the selected good events was nearly 50%.

In selecting $K_{\mu 3}$ events it is essential to remove not only the physical backgrounds but also the accidental backgrounds. The CsI(Tl) crystals suffered from accidental hits of charged particles as well as photons associated with π^+ contamination in the beam. Figure 14 shows typical CsI(Tl) detector spectra. The $M_{\gamma\gamma}$ spectrum for the 2γ events has a tail extending to the lower mass side due to the large lateral leakage of the shower. The tail part
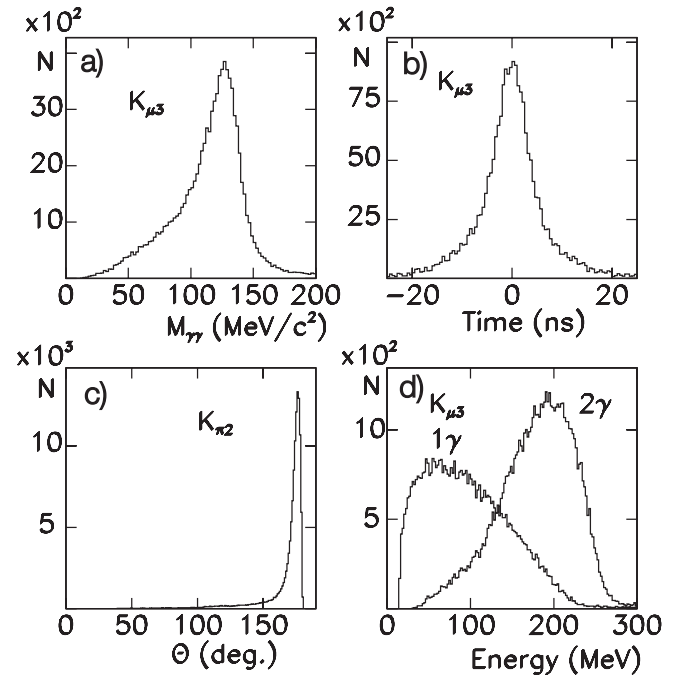

FIG. 14. Typical performance of the CsI(Tl) π^0 detection. (a) two photon invariant mass spectrum of $K_{\mu 3}$, (b) cluster timing distribution also of $K_{\mu 3}$ events showing the time resolution, (c) opening angle distribution of $K_{\pi 2}$ showing the angular resolution, and (d) two photon and one photon energy spectra of $K_{\mu 3}$ events.

has a relatively large fraction of accidentals. Thus, a proper selection of the $M_{\gamma\gamma}$ region was essential to reduce the contamination of accidentals in the 2γ events. A similar consideration was applicable to the γ energy spectra, $E_{\gamma_1} + E_{\gamma_2}$ and E_γ for the 2γ events and 1γ events, respectively, as is described in the individual analyses A1 and A2.

2. Definition of fwd and bwd events

Selected 2γ and 1γ events were separately processed in order to correct P_T for the attenuation factor. In the main P_T analysis, we used only the events with a π^0 or γ (2γ events and 1γ events, respectively) going in the *fwd* or *bwd* directions relative to the beam axis. These regions were defined in terms of the angle

$$\cos\theta_{\pi^0,\gamma} = \frac{\vec{p}_{\pi^0,\gamma} \cdot (\vec{p}_\mu \times \vec{n}_{\rm gap})}{|\vec{p}_{\pi^0,\gamma}| \cdot |(\vec{p}_\mu \times \vec{n}_{\rm gap})|}, \qquad (19)$$

where $\vec{n}_{\rm gap}$ is the magnet-gap normal unit vector. The regions of $\cos\theta_{\pi^0,\gamma} > 0.342$ and $\cos\theta_{\pi^0,\gamma} < -0.342$ were taken to be the *fwd* and *bwd* regions, respectively. This choice was determined by the sensitivity optimization of $P_T\sqrt{N_{fwd(bwd)}}$ using a Monte Carlo calculation which obtained the same value in A1 and A2. Since the attenuation in the case of one photon events is multiplicative, the same optimum conditions for 2γ and 1γ events were obtained. These angles corresponded to the polar angles of $\theta_{\pi^0,\gamma} = 70°$ and $\theta_{\pi^0,\gamma} = 110°$, respectively, for muons going exactly normal to the beam axis.

3. Positron time spectrum analysis

The time spectrum of decay positrons of the selected events was analyzed up to $19.5\ \mu$s. The time origin here is the timing of the TOF2 counter in front of the muon stopper which had the best time resolution. To make sure that muons are stopped in the Al stopper a fiducial region was defined as $|y(C4)| < 9.0$ cm and veto conditions were imposed on the stopper-surrounding anticoincidence counters. The background hits in the positron counters from the target/beam region were vetoed by shield counters as well as by the beam hodoscope B0.

There was still a significant constant background remaining primarily due to neutral particles associated with the beam. The flatness of this constant background was carefully checked and confirmed in the later part of the spectrum by fitting the time spectrum with the hypothetical function of

$$N(t) = N_0 \exp\left(-\frac{t}{\tau_\mu}\right) + b, \qquad (20)$$

with the muon mean lifetime of $\tau_\mu = 2.2\ \mu$s and a constant background b. At the beginning of the spectrum one sees a wiggle due to the spin precession of the P_L component. However, this structure is symmetric for *cw* detection

and *ccw* detection; thus it has no influence on the asymmetry measurement. The wiggle damps rapidly because of the large field inhomogeneity at the stopper. After this wiggle the spectrum was well fit by Eq. (20).

The number of signal positrons, S, was extracted from the integration of the time spectra from 30 ns to $6.0\ \mu$s by subtracting the constant backgrounds. The common upper bound of $6\ \mu$s was determined so as to give the smallest statistical error of the signal δS on average although it was slightly dependent on runs with different background levels. The error is $\delta S = \sqrt{(\delta N)^2 + (\delta B)^2}$, where N is the total number of events and B is the subtracted total background, namely $S = N - B$. In order to obtain the highest accuracy, b was deduced by fitting the spectrum from $6\ \mu$s to $19.5\ \mu$s to Eq. (20) with reduced χ^2's of typically 0.9 to 1.2. Then, B was calculated as $B = b \times n_{\rm ch}$ and $\delta B = \delta b \times n_{\rm ch}$ with the relevant number of channels, $n_{\rm ch}$ [58].

B. Method of data quality check

1. Null asymmetry check

One of the most important measures of the data quality is the "null asymmetry" A_0, which is the positron asymmetry before taking the ratio between *fwd* and *bwd*. A_0 is defined using the background-subtracted number of positron counts of *cw* and *ccw* emission for *fwd* and *bwd* events as

$$A_0 = \frac{N_{ccw}^{fwd} + N_{ccw}^{bwd} - N_{cw}^{fwd} - N_{cw}^{bwd}}{N_{ccw}^{fwd} + N_{ccw}^{bwd} + N_{cw}^{fwd} + N_{cw}^{bwd}} \qquad (21)$$

This is nearly equal to $A_0 \sim (A^{fwd} + A^{bwd})/2$ while the T-violating asymmetry is $A_T = (A^{fwd} - A^{bwd})/2$, where A^{fwd} and A^{bwd} are calculated as

$$A^{fwd(bwd)} = \frac{N_{ccw}^{fwd(bwd)} - N_{cw}^{fwd(bwd)}}{N_{ccw}^{fwd(bwd)} + N_{cw}^{fwd(bwd)}}. \qquad (22)$$

The misalignments of the positron counters and that between the polarimeter and chambers (C3 and C4) systems may give rise to a finite value of A_0. An asymmetric kaon distribution in the target may result in a shifted muon stopping distribution and inclined in-plane polarization in each stopper and thus produce $A_0 \neq 0$ when measured gap by gap; this can be canceled out by taking a sum of the 12 gaps. If it deviates from zero too much due to some systematics, the fwd/bwd scheme may not completely cancel the residual effects, although a cancellation power (reduction of the asymmetry bias at fwd/bwd subtraction) of typically 20 to 40 was confirmed in a Monte Carlo simulation with conceivable origins such as counter misalignments and asymmetric kaon stopping distribution, by entering exaggerated effects.

2. Normal asymmetry check

The positron asymmetry associated with the in-plane T-conserving polarization, A_N, is a good measure of the polarimeter sensitivity. Any admixture of background would result in its attenuation. There are two ways to measure A_N. One is to select the events with π^0s going transversely in *left* and *right* directions within finite cones, and to define $A_N = (A_{\text{left}} - A_{\text{right}})/2$. This asymmetry has the merit of having the largest value and is used in some parts of the analysis. However, in the final analyses (including the combination analysis) a different definition of

$$A_N = \frac{A_{FL} - A_{FR} + A_{BL} - A_{BR}}{4} \tag{23}$$

was adopted with the *left*(L) and *right*(R) asymmetries of the *fwd*(F) and *bwd*(B) going pions [each asymmetry was calculated by Eq. (22)] using the same events used for *fwd-bwd* T-violating asymmetry analysis. It is noted that $A_T \sim (A_{FL} + A_{FR} - A_{BL} - A_{BR})/4$. The background condition here is more realistic. A_N also includes the effect of P_N smearing $\langle\cos\theta_N\rangle$ when projected on the polarimeter axis due to the finite kinematical acceptance for the π^0s and γs. Since the definition of L and R for 1γ events is in terms of the direction of the relevant photon, there is a substantial attenuation for these events.

3. Attenuation coefficient

Since π^0/γs are detected with finite ranges in the *fwd* and *bwd* directions, there is a distribution in the decay plane. When the polarization is measured in the polarimeter reference frame, there is an attenuation of the polarization component P_T as well as P_N [59]. Thus, the observed T-violating asymmetry is

$$A_T = \alpha P_T \langle\cos\theta_T\rangle, \tag{24}$$

where α is the analyzing power determined by the polarimeter structure, and the attenuation coefficient $\langle\cos\theta_T\rangle$ is the average of the angles $\cos\theta_{\pi^0,\gamma}$ [Eq. (19)] measured event by event also taking into account the small angles of the muons relative to the gap axis. The presence of accidental backgrounds reduces not only the polarization but also $\langle\cos\theta_T\rangle$ from the value for a pure event case which can be calculated with a Monte Carlo simulation. This reduction factor η, when written as $A_T = \alpha P_T \eta \langle\cos\theta_T\rangle_{\text{MC}}$ is also relevant for the A_N measurement and can be regarded as common. Namely,

$$A_T = \frac{P_T}{P_N} A_N \frac{\langle\cos\theta_T\rangle}{\langle\cos\theta_N\rangle} = \frac{P_T}{P_N} A'_N. \tag{25}$$

Thus, not only the intrinsic polarimeter sensitivity but also the data quality is regarded as proportional to the corrected in-plane asymmetry A'_N.

4. Decay-plane rotation check

The symmetry of the decay phase space of selected events can be checked in terms of the decay plane distribution. The average angle of the decay planes (called "decay-plane rotation") is a measure of the phase space distortion. Imperfect detector efficiency and any failure in data analysis unfavorable to some kinematic region may result in such a distortion. If one looks at one of the gaps there should be significant rotation, for example, due to the asymmetric kaon stopping distribution in the target. The decay-plane rotation is thus an overlapping check in addition to A_0. The two angle components of the decay plane were calculated as

$$\cos\theta_r = \vec{n}_r \cdot \frac{\vec{n}_{\mu^+} \times \vec{n}_{\pi^0}}{|\vec{n}_{\mu^+} \times \vec{n}_{\pi^0}|} \tag{26a}$$

$$\cos\theta_z = \vec{n}_z \cdot \frac{\vec{n}_{\mu^+} \times \vec{n}_{\pi^0}}{|\vec{n}_{\mu^+} \times \vec{n}_{\pi^0}|}, \tag{26b}$$

where $\vec{n}_r$ and $\vec{n}_z$ are the unit vectors of the Cartesian coordinate system of the polarimeter. Associated with these decay-plane rotations, spurious effects of P_T are induced due to the admixture of P_N and P_L, respectively. They can be calculated using their average values $\langle\theta_r^{fwd}\rangle$ and $\langle\theta_z^{fwd}\rangle$ as

$$\delta P_T^r = \tfrac{1}{2}(\langle\theta_r^{fwd}\rangle - \langle\theta_r^{bwd}\rangle)P_N \tag{27a}$$

$$\delta P_T^z = \tfrac{1}{2}(\langle\theta_z^{fwd}\rangle + \langle\theta_z^{bwd}\rangle)P_L. \tag{27b}$$

C. Analysis A1

1. Event selection

(a) Cut-point optimization.—One of the main features of the analysis A1 was the cut-point determination guided by the figure-of-merit optimization. Namely, for each cut variable the sensitivity for Imξ was calculated and maximized. Narrower selection means a smaller background admixture but fewer events resulting in a smaller statistical significance. The figure of merit (FoM) was evaluated as

$$\text{FoM} = A_T N_{K_{\mu3}}/\sqrt{N_{K_{\mu3}} + 2N_{BG}}, \tag{28}$$

where the asymmetry A_T and statistical sensitivity are estimated by a Monte Carlo simulation (see below) taking into account the backgrounds from $K_{\pi2}$ and accidentals. This method of routine cut-point determination has the advantage that human bias is reduced, but on the other hand, it admits a small admixture of backgrounds, even if it has a δP_T bias. Therefore, in practice, the cut-point dependence of A_N and A_T^{biased} (see below) was checked to verify its insignificance. Among the runs in each of the three data sets, the cut conditions were unchanged.

(b) Principle of blind analysis.—Another feature of the A1 analysis was the adoption of a blind analysis technique.

One did not look at the P_T (or A_T) result throughout (i) the cut-point optimization, (ii) data quality check by means of A_0, A_N, and $\cos\theta_T$, and (iii) the systematics check in terms of decay-plane distribution. Even for the check of A_T dependences on cut conditions, an unknown random bias was artificially added to the real A_T in the computer code as $A_T^{\mathrm{biased}} = A_T + \mathrm{bias}$, and only after all the necessary processes were finished, the real A_T was revealed by opening the unknown bias box.

(c) Three point tracking.—A distinct difference between both analyses was in the charged particle tracking. In A1 only the chambers C2, C3, and C4 were used to reconstruct a track and extract the momentum. In this way it was intended to perform reliable fitting without using the elements of target/ring which had poor resolutions. These elements only served for consistency checks between the hit point and the fit point.

(d) Monte Carlo simulation.—For the cut-point optimization and other necessary simulations, a Monte Carlo code GMC was developed based on GEANT3 [60]. In order to reproduce the realistic experimental condition, it was essential to incorporate not only the physics but also the accidental backgrounds especially in the Cs(Tl) calorimeter. The pattern of accidental hits could be well simulated experimentally by using $K^+ \rightarrow \mu^+ \nu$ ($K_{\mu2}$) events in the prescaled mixed trigger without requiring a CsI(Tl) signal.

2. CsI(Tl) analysis

(a) Hit CsI(Tl).—The CsI(Tl) analysis proceeded in the following way. First, hit modules were identified as having good timing relative to the fiducial counter trigger timing. A typical timing distribution is shown in Fig. 14(b). Next, a cluster was formed according to a clustering algorithm, deducing a photon hit. The timing gates on crystals were determined to cover about $\pm 4\sigma$ of the distribution [52] which is dependent on the energy deposited and also slightly on the beam periods. The gates were not changed throughout each data set.

(b) CsI(Tl) clustering.—In order to form a cluster, a seed module was selected as a module having $E > 5$ MeV and good timing. Neighboring modules were joined if they had good timing in the case of $E > 5$ MeV. Modules without good timing were also added if their energy was low ($E < 5$ MeV). The TD was used to correct the energy for pileup in the 1996–1997 data analysis but this was not employed later because the photon energy improvement was not very significant. A cluster was redefined as 3×3 modules having the maximum energy and its photon timing (T_c) was calculated as the weighted average of those 9 modules as

$$T_c = \left(\sum w_i T^i\right) \Big/ \sum w_i \tag{29a}$$

$$w_i = 1/\sigma_i^2(E_i), \tag{29b}$$

where T_i is the timing of ith module and $\sigma(E_i)$ is the module timing width at the energy deposit of E_i. The energy of the cluster was calculated as the sum energy of the 9 crystals and a gate was also set. T_c is a good measure to identify a good signal cluster. The energy deposit distribution among the 9 crystals is also sensitive to accidental backgrounds. In order to use this property to remove the accidentals, the standard deviation of T_c was checked by means of

$$W_c = 1 \Big/ \sqrt{\sum w_i}. \tag{30}$$

It was found that there is a correlation between a large T_c/W_c ratio and the accidental beam hit events and thus a cut was set on this variable. The ratio of 2γ events and 1γ events at this stage was roughly one to one with a significant fraction (several percent) of more than two clusters exhibiting a non-negligible amount of accidental hit events in both the 2γ and the 1γ data.

(c) Cut conditions for 2γ and 1γ.—Several cuts on the π^0 decay kinematics were effective to reject those accidentals. For events with more than two clusters, a combination with the best $M_{\gamma\gamma}$ was assigned to be the pair from the π^0. Three conditions were required: (i) the sum of photon energies is $E_{\gamma_1} + E_{\gamma_2} > 100$ MeV, (ii) the opening angle of the two γ's is $\theta_{\gamma\gamma} > 49.5°$, and (iii) the 2γ invariant mass should be 75 MeV $< M_{\gamma\gamma} < 180$ MeV. The typical spectra of $M_{\gamma\gamma}$, $E_{\gamma_1} + E_{\gamma_2}$ for 2γ, E_γ for 1γ are shown in Fig. 14. The lower bound of $M_{\gamma\gamma}$ was lowered to 65 MeV for the Data II, and the mass window was further narrowed to $85 < M_{\gamma\gamma} < 150$ MeV/c^2 for Data III. These windows were determined mainly by looking at A_N and A_T^{biased} differential behavior and taking their constant regions; the larger fraction of background contamination in the tail regions resulted in deviations of A_N and A_T^{biased}. Because the beam condition for run III was not good and the intensity was higher, the $M_{\gamma\gamma}$ window had to be tighter. For 1γ events a condition on energy $70 < E_\gamma < 220$ MeV was applied. The parameters of π^0 analysis are summarized in Table III.

3. Charged particle analysis

(a) K^+ stopping.—The energy threshold of each target fiber was set to 10 MeV. Figure 10 shows the time spectrum of the fiber with maximum energy deposit. In order to assure K^+ stopping, normally $t_K > 3$ ns and $t_K > 4$ ns were selected for 2γ and 1γ events, respectively ("normal cuts"). However, the respective regions of $2 < t_K < 3$ ns and $3 < t_K < 4$ ns were also saved with the stronger kinematical constraints (see below) as "tight events."

(b) Chamber analysis.—The cathode signals of C2, C3, and C4 were analyzed to deduce the hit positions. The charge ratio method was employed to analyze the cathode signals. A look-up table was referenced for the ratio
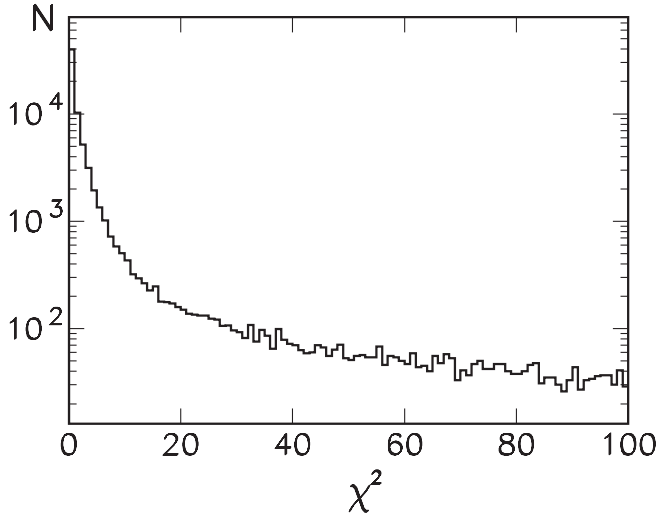
FIG. 15. χ^2 distribution of charged particle tracking in the A1 analysis

FIG. 16.   Track consistency check at ring (top) and target (bottom).

$R = (q_0 - q_{+1})/(q_0 - q_{-1})$ to determine a position, where q_0 is the maximum induced charge among strips and q_{+1} and q_{-1} are those of adjacent strips. The table was made for various incident angles because an offset was significant for oblique incidence. For all the chambers the typical hit multiplicity was less than 2.

   (c) Track fitting.—The track fitting using the three chambers C2, C3, and C4 was performed by means of a quality check by

$$\chi^2 = \sum_{i=1}^{6}\left(\frac{x_i^{\text{hit}} - x_i^{\text{fit}}}{\sigma_i}\right)^2. \qquad (31)$$

Here, x_i^{hit} and x_i^{fit} are the actual hit position and the track fit point of the chamber coordinate i, and σ_i is its resolution. Figure 15 shows the χ^2 distribution of fitted trajectories, on which a cut was set at $\chi^2 = 10$ for Data I and 5.5 later. Using this cut some of the π^+ decay-in-flight background could be removed. Also a single correct track was selected for chamber multihit events. In the track fitting multiple scattering was taken into account in the 1998 to 2000 analyses. The fit trajectory was extrapolated to the target/ring and the distance to the hit fiber was analyzed (Fig. 16). A cut was applied such that $\delta r = \sqrt{\Delta x^2 + \Delta y^2} < 2.0$ cm, and $\Delta z < 2.5$ cm, separately for target and ring in the 1996–1997 analysis, but combined simply such that $\delta l = \sqrt{\Delta x^2 + \Delta y^2 + \Delta z^2} < 2.0$ cm in the later analysis. The extracted momentum distribution is shown in Fig. 11 justifying the selection of $p < 190$ MeV.

   (d) TOF analysis.—The particle identification was done by TOF. The TOF2 counter timing (stop timing) was defined as an average of timings of two PMTs at the outer and the inner ends of the counter as $t_2 = (t_{\text{in}} + t_{\text{out}})/2$ while the start timing by the fiducial counter with one-end readout was deduced as $t_1 = t_{\text{Fid}} + x/c_n$, where x is
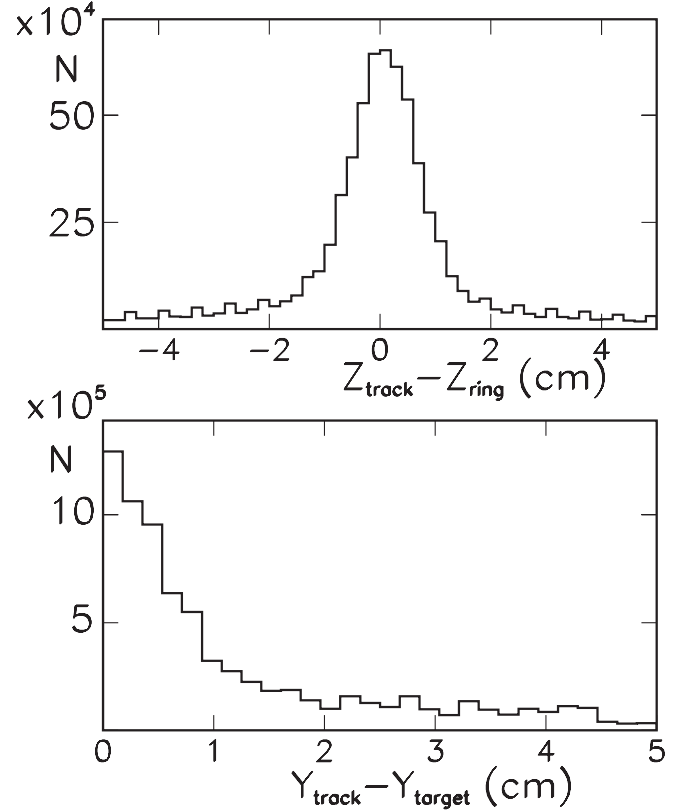
the hit position and c_n is the effective light velocity in the counter; $c_n = 18$ cm/ns was obtained from a calibration measurement. Time-walk corrections were applied to both t_1 and t_2. By using the time difference $\Delta t = t_2 - t_1 + \delta t$ and the flight length and momentum deduced from the track fitting, the velocity was analyzed in terms of Eq. (18). Here the instrumental offset δt could be extracted for μ^+ and π^+ using $K_{\mu 2}$ and $K_{\pi 2}$ monochromatic signals, respectively. The separation between μ^+ and e^+ is sufficient in the M_{TOF}^2 spectrum (Fig. 12). The events with $3500 < M_{\text{TOF}}^2 < 18\,000$ (15 000 for Data III) (MeV/c^2)^2 or $5000 < M_{\text{TOF}}^2 < 15\,000$ (MeV/c^2)^2 were accepted for the normal and tight kaon timing, respectively. The parameters of charged particle analysis are summarized in Table IV.

4. Kinematical cuts and others

   In order to ensure kaon decays at rest and to reject backgrounds (accidentals as well as physical ones) several kinematical constraints were useful. The $K_{\pi 2}$ pions and its decay-in-flight muons have a nearly back-to-back condition for the μ^+ and the π^0 decay photons, and thus the conditions of $\theta_{\mu^+\pi^0} < 160°$ and $\theta_{\mu^+\gamma} < 150°$ were applied for 2γ and 1γ events, respectively. The missing mass which was defined as
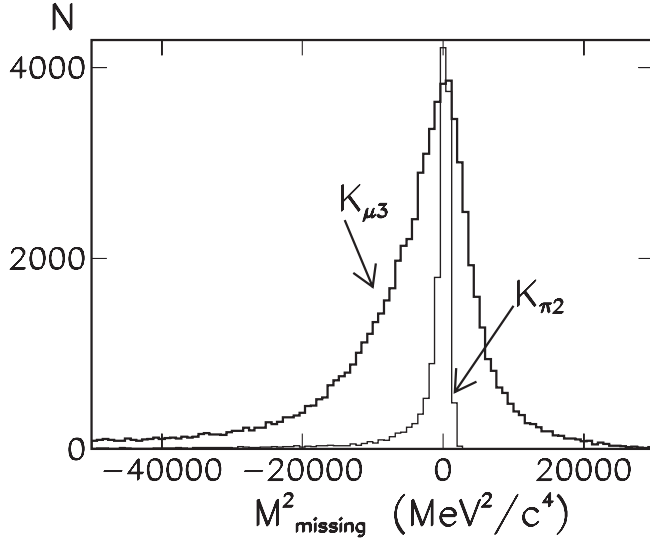
FIG. 17. Missing mass distribution for $K_{\mu 3}$ and $K_{\pi 2}$ events.

$$M_{\rm miss}^2 = (M_{K^+} - E_{\mu^+} - E_{\pi^0})^2 - (\vec{p}_{\mu^+} + \vec{p}_{\pi^0})^2 \quad (32)$$

was effective to ensure the $K_{\mu 3}^+$ decay of stopped kaons for 2γ events in the target tight cut region. The condition of $M_{\rm miss}^2 > -5000 \ ({\rm MeV}/c^2)^2$ and $\theta_{\gamma\gamma} > 65°$ was also imposed (Fig. 17). For 1γ events a similar cut was applied on the correlation plot of photon energy, E_γ, and muon-photon opening angle, $\theta_{\mu^+\gamma}$, two-dimensionally.

5. Systematics checks and A_T

After the event selection of each beam cycle, several checks were performed. First, the null asymmetry A_0 as defined in Eq. (21) was confirmed to be ≈ 0. Second, the attenuation factor $\langle\cos\theta_T\rangle$ calculated as Eq. (19) (Table V) was checked to be consistent with the Monte Carlo value. Third, the detector sensitivity A_N was controlled [61]. The cut-point dependences were studied to confirm the proper choice of the cut points to reach the highest sensitivity. This study was done for $M_{\gamma\gamma}$ and E_γ for 2γ and 1γ, respectively, as well as $M_{\rm TOF}^2$. The decay-plane rotation was confirmed not to deviate from zero. Then finally, $A_T^{\rm biased}$ dependence on variables was checked not to have a strange behavior. These studies were done for the y coordinate of C4 ($C4y$), $M_{\gamma\gamma}(2\gamma)$, $E_\gamma(1\gamma)$, the hit/fit differences of target/ring, χ^2, $M_{\rm miss}^2$, $\theta_{\mu^+\pi^0}(2\gamma)$, $\theta_{\mu^+\gamma}(1\gamma)$ and t_K. After all these systematics checks were completed, the unknown *bias* was revealed.

6. Backgrounds

There are four sources of backgrounds appearing in this experiment: (i) accidental hits in the Cs(Tl), (ii) decay-in-flight of $K_{\pi 2}$ pions, (iii) kaon decay-in-flight, and (iv) accidental hits in the positron counters. Although the K_{e3} background in the same momentum region was re-

moved by TOF, a small tail fraction contributed to the prompt part of the e^+ time spectrum when a scattered e^+ from the stopper hits the positron counter. The contamination fraction of (i), (ii), and (iii) was carefully estimated in Data set I, because it was the worst case of accidental rates; the periods II and III had tighter cut conditions and the contaminations were less.

The accidental CsI(Tl) hits could be studied by using the data taken by the prescaled trigger. By selecting $K_{\mu 2}$ events which should have no photon, the rate and hit pattern could be investigated and the fraction in the selected events was estimated to be 9.6% for 2γ and 4.5% for 1γ. The π^+ decay-in-flight background was dangerous because of its potential transverse muon polarization. However, this background could be well reproduced in a Monte Carlo simulation and it was estimated to be 2.4% for 2γ and 4% for 1γ events. The admixture of the kaon decay-in-flight background was very dependent on the cut conditions on the target timing spectrum. It is significant in the *fwd* events but not so in the *bwd* events. In order to estimate the contamination fraction, a sample of very pure $K_{\pi 2}$ events with no kaon decay-in-flight contamination and with monochromatic momentum was first extracted. Then, its target timing spectrum was subtracted from a $K_{\mu 3}$ time spectrum, leaving a distinct prompt peak in the *fwd* spectrum. In this way fractions of 1.55% (0.19%) for 2γ and 1.71% (0.32%) for 1γ were obtained (Table VI). The accidental hits in the positron counters could not be avoided because of the very long gate for e^+ detection. However, this background could be evaluated since it produced a flat constant component in the positron time spectrum.

D. Analysis A2

1. Event selection

(a) Cut-point optimization. —The event selection criteria in the analysis A2 were also based on FoM optimization. In contrast to A1, in which the figure-of-merit calculation relied on Monte Carlo simulations, it was aimed to estimate it from experimental data as much as possible. The FoM was defined as

$$\text{FoM} = A_N^{\rm exp}\sqrt{N_{\rm left/right}}, \quad (33)$$

where $A_N^{\rm exp} = (A_{\rm left} - A_{\rm right})/2$ is the normal in-plane asymmetry experimentally measured for the normal cones, and $N_{\rm left/right}$ is the number of events. This FoM using experimental data was adopted to be free from any possible errors due to assumptions in the simulation. The disadvantages, on the other hand, are the statistical accuracy which is limited by the data, and the use of the π^0 event regions which are not relevant to the P_T analysis, namely *fwd/bwd* regions. In the case where the FoM maximum was not uniquely determined, rather tight cuts were preferred and these were adopted in the analysis of the 1996–

1997 data. However, after confirming the goodness of the selected data, the cut conditions were loosened to accept more events in the later analyses resulting in a larger acceptance. The data quality checks in terms of A_0, A_N, and $\langle\cos\theta_T\rangle$ were done as in A1. The cut-point dependence of A_T (or P_T) was investigated only in a global way by comparing the values in subdivided regions.

(b) Monte Carlo simulation.—A Monte Carlo code different from A1 was employed to simulate the data. It is also based on GEANT3. The prime purpose of the calculation was to estimate the analyzing power α and the sensitivity function $\langle P_T/\mathrm{Im}\xi\rangle$ and attenuation factor $\langle\cos\theta_T\rangle$. The spectra of kinematic variables were compared with the simulation results. As in A1 a realistic condition of the CsI(Tl) accidental backgrounds was taken into account utilizing the hit pattern of the prescaled $K_{\mu2}$ events.

2. CsI(Tl) analysis

(a) CsI(Tl) crystal timing.—As in A1 the timing gate was set on each crystal depending on the energy deposited, typically covering the distribution peak with $\pm4\sigma$ width. In total 8 energy steps were defined. For example, above 75 MeV a gate of ±15 ns was used. The set of gates was finely tuned for each data period. For Data I, a time-walk correction was not applied with the consequence of asymmetric timing distributions, but for II and III this correction was employed and symmetric and narrower distributions were realized. The gates in Data I were set rather narrow to remove accidental hits but this deteriorated the energy resolution of a signal event due to the loss of constituent crystals in a cluster. For II and III the crystal gates were opened wider and tighter constraints were imposed on the timing of clusters as described below.

(b) CsI(Tl) clustering.—Clustering was performed in the following way. First, a seed crystal was selected as any crystal with good timing and energy more than 5 MeV. Then neighboring crystals with good timing regardless of their energy deposit were joined to the cluster to form a 3×3 matrix which had the maximum energy. The TD information was not used in the analysis. The timing of the cluster was defined as the simple average of the crystals of the 3×3 matrix in Data I but the same definition [Eq. (29)] as A1 was adopted to increase the rejection of accidental events. Also, constraints were imposed on the timing depending on the energy of cluster E_{cl}. The clusters with bad timing were rejected as coming from background. Clusters with energy in the ranges $20 < E_{\mathrm{cl}} < 250$ MeV, $15 < E_{\mathrm{cl}} < 250$ MeV, and $30 < E_{\mathrm{cl}} < 300$ MeV for Data I, II, and III, respectively, were accepted as photons.

(c) Cut conditions for 2γ and 1γ.—In order to purify π^0 events several constraints were imposed on the $\pi^0 \to \gamma\gamma$ decay kinematics as in A1. The parameters and cut conditions were optimized for each data period and they are summarized in Table III. For 2γ events not only (i) a cut on the energy sum of two photons, $E_{\mathrm{sum}} = E_{\gamma_1} + E_{\gamma_2}$, but

TABLE III. Summary of π^0 analysis for three data periods of I (1996–1997), II (1998), and III (1999–2000) in the analyses A1 and A2.

	Data period	I	II	III
A1	$= 2\gamma$ events $=$			
	E_{sum} (MeV)	>100	>100	>100
	$M_{\gamma\gamma}$ (MeV/c^2)	75–180	65–180	85–150
	$\theta_{\gamma\gamma}$	$>49.5°$	$>49.5°$	$>49.5°$
	$= 1\gamma$ events $=$			
	E_γ (MeV)	70–220	70–220	70–220
A2	$= 2\gamma$ events $=$			
	E_γ (MeV)	>20	>15	>15
	E_{sum} (MeV)	20–250	15–270	15–270
	$M_{\gamma\gamma}$ (MeV/c^2)^2	75–160	75–170	75–170
	$\theta_{\gamma\gamma}$	$>60°$	$>50°$	$>65°$
	$= 1\gamma$ events $=$			
	E_γ (MeV)	70–250	70–250	70–250

also (ii) a cut on each photon energy E_γ was set. The cut condition of E_{sum} was conservative in I but loosened in II and III resulting in larger acceptance with more final statistics. In cases where there are more than two clusters, a pair with the best cluster timing was identified as the π^0, while the invariant mass $M_{\gamma\gamma}$ was the combination criterion in A1. (iii) The two photon opening angle was required to be larger than a certain value of $\theta_{\gamma\gamma}$ similar to A1; (iv) the two γ invariant mass $M_{\gamma\gamma}$ was chosen in a range to diminish the accidental background contamination. It was also conservative in I ($75 < M_{\gamma\gamma} < 160$ MeV/c^2) but loosened in II ($75 < M_{\gamma\gamma} < 170$ MeV/c^2) and in III ($65 < M_{\gamma\gamma} < 220$ MeV/c^2). For 1γ events $E_\gamma > 70$ MeV was imposed.

3. Charged particle analysis

(a) Four element tracking.—In the charged particle tracking two dimensional coordinates of four elements were used in fitting; namely, the combination of the r (or x and y) coordinates from the target and z coordinate from the ring scintillator, and the three chambers C2, C3, and C4. This makes a distinct contrast to the 3 element fitting of A1. Although the resolution of the target/ring counters is much worse than that of the other chambers and the absolute coordinate system of the target/ring system may have a small offset from that of the chamber system due to the mechanical structure of the setup, the χ^2 was very effective in eliminating the $K_{\pi2}$ backgrounds. Here χ^2 is defined as

$$\chi^2 = \sum_{i=1}^{6}\left(\frac{x_i^h - x_i^f}{\sigma_x}\right)^2 + \left(\frac{z^h - z^f}{\sigma_z}\right)^2 + \left(\frac{r^h - r^f}{\sigma_r}\right)^2, \quad (34)$$

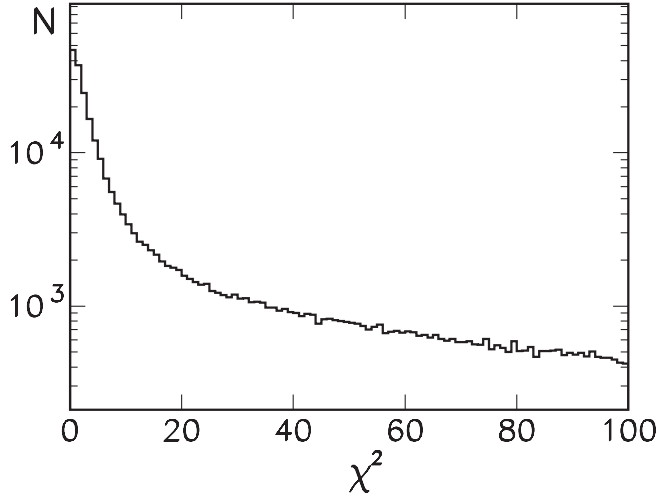where x_i are the chamber coordinates, r the target radial coordinate, and z the ring coordinate of the hit (h) and

FIG. 18. χ^2 distribution of charged particle tracking in the A2 analysis.

TABLE IV. Summary of μ^+ analysis for the three data periods of I (1996–1997), II (1998), and III (1999–2000) in the analyses A1 and A2.

	Data period	I	II	III
	p_μ (MeV/c)	<190	<190	<190
	M^2_{TOF} (MeV/c^2)^2	3500–18 000	3500–18 000	3500–15 000
	$\theta_{\gamma\gamma}$	$>49.5°$	$>49.5°$	$>49.5°$
A1	Tracking			
	χ^2	<10	<5.5	<5.5
	Target (cm)	$\delta r < 2.0$	$\delta r < 2.0$	$\delta l < 2.0^{\text{a}}$
	Ring (cm)	$\delta z < 2.5$	$\delta z < 2.5$	$\delta l < 2.0^{\text{a}}$
	p_μ (MeV/c)	<190	<190	<190
	$M^2_{\text{TOF}}/\frac{dE}{dx}$	2 dimension	2 dimension	2 dimension
A2	Tracking χ^2			
	2γ	<20	<20	<20
	1γ	<10	<10	<10

$^{\text{a}}\delta l = \sqrt{\delta r^2 + \delta z^2}$.

fitted (f) positions. The χ^2 distributions of a typical data run are shown in Fig. 18. The cuts $\chi^2 < 20$ and $\chi^2 < 10$ were selected for 2γ and 1γ events, respectively. Figure 19 shows how the $K_{\pi2}$ backgrounds, which have the back-to-back π^0-μ^+ correlation, could be eliminated by the χ^2 cut. The obtained momentum spectrum is similar to Fig. 11 and the region $p < 190$ MeV/c was selected as the $K_{\mu3}$ region. All the tracking parameters are summarized in Table IV.

(b) Analysis of tracking elements.—As in A1 a charge-ratio method was used to deduce a hit point from the cathode signals. Because the cathode signals were not calibrated run by run the position resolution was a little inferior to the analysis in A1, but there was no significant difference in the momentum resolution.
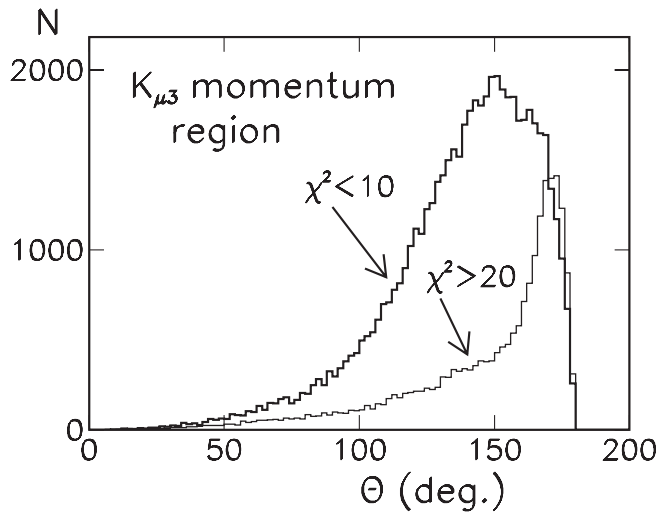

FIG. 19. Opening angle $\theta_{\mu\pi(\gamma)}$ distribution of the $K_{\mu3}$ decay region ($p < 190$ MeV) for $\chi^2 < 10$ and $\chi^2 > 20$ of 2γ events. It is seen that $K_{\pi2}$ background with back-to-back correlation is concentrated in the large χ^2 region.

(c) TOF analysis.—The analysis process is essentially the same as in A1, but it was performed on the two-dimensional space of M^2_{TOF} and ΔE, the energy deposited in the TOF2 counter.

4. Kinematical cuts and others

Several kinematical cuts were applied as in A1. To assure a kaon stop and avoid decay-in-flight events the selection of delayed decays in the kaon decay time spectrum was essential and $t_K > 3$ ns was the basic condition. Here a kinematical constraint of $-25\,000 < M^2_{\text{miss}} < 25\,000$ (MeV/c^2)^2 was applied. However, to save events near the prompt timing with $t_K < 3$ ns, the events with one of the following conditions were accepted for 2γ: (i) one of the target fiber energy deposits is large enough ($E > 3000$ ADC bin [62]), (ii) the muon momentum is low enough ($p_{\mu^+} < 180$ MeV/c), (iii) the opening angle of the π^0 decay into two γ's is large enough ($\theta_{\gamma\gamma} > 65°$), or (iv) the missing mass is not large ($M^2_{\text{miss}} > -20000$ (MeV/c^2)^2). For 1γ, the events in the $t_K < 3$ ns region were also accepted if (i) the target energy deposit is large ($E > 3000$ ADC bins), (ii) the muon momentum is small ($p_\mu < 175$ MeV/c), or (iii) the photon energy is small ($E_\gamma < 180$ MeV). These conditions were determined from Monte Carlo studies.

5. Systematics checks and A_T

Data quality checks using A_0 and $\langle\cos\theta_T\rangle$ are summarized in Table V. The decrease of $\langle\cos\theta_T\rangle$ for the 1γ events for II and III was due to the loosened cut conditions. For these, the deviation of A_0 from zero is significant. The obtained A_T's are mostly consistent with zero with one exception of 1γ events in data set II with a 2.3σ effect. However, this effect was found to have a correlation with the difference of the muon stopping distributions between

TABLE V. Number of selected events N, null asymmetry A_0, attenuation factor $\langle\cos\theta_T\rangle$, and obtained T-violating asymmetry A_T for three data periods of I (1996–1997), II (1998), and III (1999–2000).

Data period	I	II	III
= 2γ events =			
N(10^6)	1.07	0.80	0.92
$A_0 \times 10^3$	2.29 ± 1.05	-1.15 ± 1.23	-1.23 ± 1.14
$\langle\cos\theta_T\rangle$	0.771	0.761	0.724
$A_T \times 10^3$	-0.09 ± 1.08	0.69 ± 1.23	-0.79 ± 1.15
A1			
= 1γ events =			
N(10^6)	0.87	0.70	0.91
$A_0 \times 10^3$	1.23 ± 1.17	-1.50 ± 1.32	-0.52 ± 1.16
$\langle\cos\theta_T\rangle$	0.633	0.769	0.579
$A_T \times 10^3$	-1.40 ± 1.17	-1.87 ± 1.31	1.17 ± 1.17
= 2γ events =			
N(10^6)	1.04	0.81	1.22
$A_0 \times 10^3$	-2.01 ± 1.12	-0.70 ± 1.1	-2.32 ± 1.10
$\langle\cos\theta_T\rangle$	0.770	0.763	0.721
$A_T \times 10^3$	0.31 ± 1.09	1.66 ± 1.02	0.01 ± 1.00
A2			
= 1γ events =			
N(10^6)	0.93	0.81	1.26
$A_0 \times 10^3$	-2.00 ± 1.18	-4.0 ± 1.2	-2.01 ± 0.99
$\langle\cos\theta_T\rangle$	0.649	0.590	0.562
$A_T \times 10^3$	-0.50 ± 1.17	-2.89 ± 1.20	0.53 ± 0.99

fwd and *bwd*, and this could be removed in the differential polarimeter analysis.

6. Backgrounds

The accidental background in the CsI(Tl) could be estimated from the prescaled trigger $K_{\mu2}$ data in the data period II in which the background condition was worst. After applying all the cuts it was found that the 1γ events contained 8.9% of accidental events. The 2γ events had 9.5% accidentals, most of which (8.0%) was due to pileup of a signal photon and an accidental CsI(Tl) hit. The contamination of $K_{\pi2}$ and its decay-in-flight was carefully investigated in the μ-$\pi(\gamma)$ opening angle spectrum (Fig. 19). This was less than 1.5% for 2γ and 2% for 1γ. The admixture of kaon decay-in-flight events could be evaluated in the kaon decay time spectrum of reliable

TABLE VI. Summary of major background fractions in percent in the analyses A1 and A2. DIF means "decay-in-flight."

	A1		A2	
Source	2γ	1γ	2γ	1γ
CsI(Tl) accidental	9.6	4.5	9.5	8.9
$K_{\pi2}$-π-DIF	2.4	4	<1.5	2
$K_{\mu3}$ from K^+-DIF	1.55	1.71	1.5	2.0

$K_{\pi2}$ events, using the difference between *fwd* and *bwd* because it contributed mainly to *fwd*. This was 2.6% and 3.6% for 2γ and 1γ, respectively, for *fwd*, and 1.5% and 2.0%, respectively, if *fwd* and *bwd* were averaged. The backgrounds are summarized in Table VI.

E. Combination of the two analyses

1. The method

(a) Evaluation of the two analyses.—The events selected in each analysis were those passing a number of cut criteria and this would provide the final result if only one analysis had been performed. The two analyses were performed independently for each data period based on slightly different analysis methods. Although their difference was not very large a number of cut applications created data sets with significantly different events. As there was no way to judge which analysis was superior, we adopted a method to respect both analyses equally and to combine the data sets from both analyses on an equal footing. Namely, all the events selected by either analysis were defined as good events and used to extract our final result.

(b) Generation of "common" and "uncommon" data sets.—First, all the selected events were sorted into three categories: (i) events selected by both A1 and A2 (*common*), (ii) events selected only by A1 (A1 *uncommon*), and (iii) events selected only by A2 (A2 *uncommon*). This resorting was done separately for 2γ and 1γ giving rise to 6 data sets in total. There were also events which were selected as 2γ in A1 but as 1γ in A2 and vice versa. These events were rejected because the fraction was small (1.5% of the total events typically) and their strict treatment was not simple. The ratio of *common* to *uncommon* events is slightly dependent on the beam period (beam condition) due to the different background conditions in the CsI(Tl) detector and different cut conditions etc., but typically the three data sets had a similar number of events. Table VII shows a summary of the number of selected events for the 6 data sets and for the three data taking periods of I, II, and III. The $2\gamma/1\gamma$ mismatch events are also listed. The positron time spectra are shown in Fig. 20.

(c) Origin of uncommon events.—The existence of uncommon events is a consequence of the cut conditions set on several kinematic variables. To illustrate this point the CsI(Tl) analysis of 2γ event is shown as an example (Fig. 21). Since the calorimeter had considerable large lateral shower leakage, the width of $M_{\gamma\gamma}$ is large extending as a tail to the lower mass region. However, the events far from the peak on the higher side as well as lower side are likely to contain a significant fraction of accidental events; thus, they were rejected. Figure 21 shows the correlation of $M_{\gamma\gamma}$ in A1 and A2. Although it shows $M_{\gamma\gamma}(A1) \sim M_{\gamma\gamma}(A2)$, the distribution is fairly wide. This is regarded as an analysis resolution. When a cut $M_{\gamma\gamma} = m_0$ was set, some events are selected either in A1 or A2. The analysis consisted of nearly 15 cut conditions, each of which re-

TABLE VII. Number of events for the combined data sets for three data periods of I (1996–1997), II (1998), and III (1999–2000).

Data period	I	II	III	Total
2γ events				
A1 · A2 *com*	772 845	765 732	737 362	2 275 939
A1 *uncommon*	716 184	517 400	605 258	1 838 842
A2 *uncommon*	591 234	676 492	891 393	2 159 119
2γ(A1)-1γ(A2)	19 912	14 570	36 012	70 494
1γ(A1)-2γ(A2)	38 965	70 693	70 100	179 758
1γ events				
A1 · A2 *com*	585 519	587 208	620 127	1 792 854
A1 *uncommon*	601 325	481 547	676 572	1 759 444
A2 *uncommon*	642 360	555 173	790 522	1 988 055
Total (2γ + 1γ)	3 909 467	3 583 552	4 321 234	11 814 253

sulted in a small percentage of uncommon events. All uncommon events were accounted for by this study.

2. Data quality check and the merits of the method

(a) General.—For the 6 data sets a quality check was performed in terms of A_0, A_N, and the decay-plane rotations, as in the individual analyses. The purpose of these checks was first to confirm that the quality of the *uncommon* data is not inferior to the *common*'s in both cases of 2γ and 1γ, and to find any errors in the data processing and analysis. The performance of the analysis codes was also cross-checked in this way. Each analysis team set its own policy and criterion for data analysis. It was each team's decision as to which run to discard for those with poor beam quality. Thus the cross-checking was effective all

through the data handling processes. Second, by looking at some quantities of the *common* events in the two analyses, the ambiguities of the analyses could be inferred. For example, the attenuation factor $\langle \cos\theta_T \rangle$, to which the final P_T is inversely proportional, was compared, thus providing rough estimates of the systematic error (ambiguity) of the analyses.

(b) Null asymmetry A_0.—The values of A_0 are summarized in Table VIII for the 18 data sets. They are mostly consistent with zero, but exceptions are relatively large deviations seen in 2γ A2-*uncommon* of I (2.6σ), 1γ *common* of II (2.5σ) and 2γ *common* of III (3.2σ). The causes for these nonzero values were not pursued, but it could be considered harmless due to the large cancellation power of the *fwd/bwd* scheme.

(c) Normal asymmetry A_N.—Significant scattering of the values among periods and data sets, especially for 1γ data, is seen because of the different accidental background levels and the different cut conditions in the analysis. In Table IX the corrected normal asymmetry A'_N [Eq. (23)] is also compared among the data sets. Here $\langle \cos\theta \rangle$ was evaluated from experimental data instead of Monte Carlo calculation because of fewer assumptions. For data sets I, we observe good agreement between the common and uncommon events. For data sets II and III there are significant tendencies that A'_N are smaller for the uncommon events. Since the likely influence of the accidental background is to decrease the asymmetry, it could be regarded as harmless. There is also a second reason. As is seen in Table IX, A'_N (or A_N) is different in A1 and A2 even for the common events. This is due to the different performance of the photon angle determination in both analyses. In fact, there are also mismatch events of A1-*L*/A2-*R* or A1-*R*/A2-*L* because the *L*- and *R*-regions are adjacent in the *fwd* and
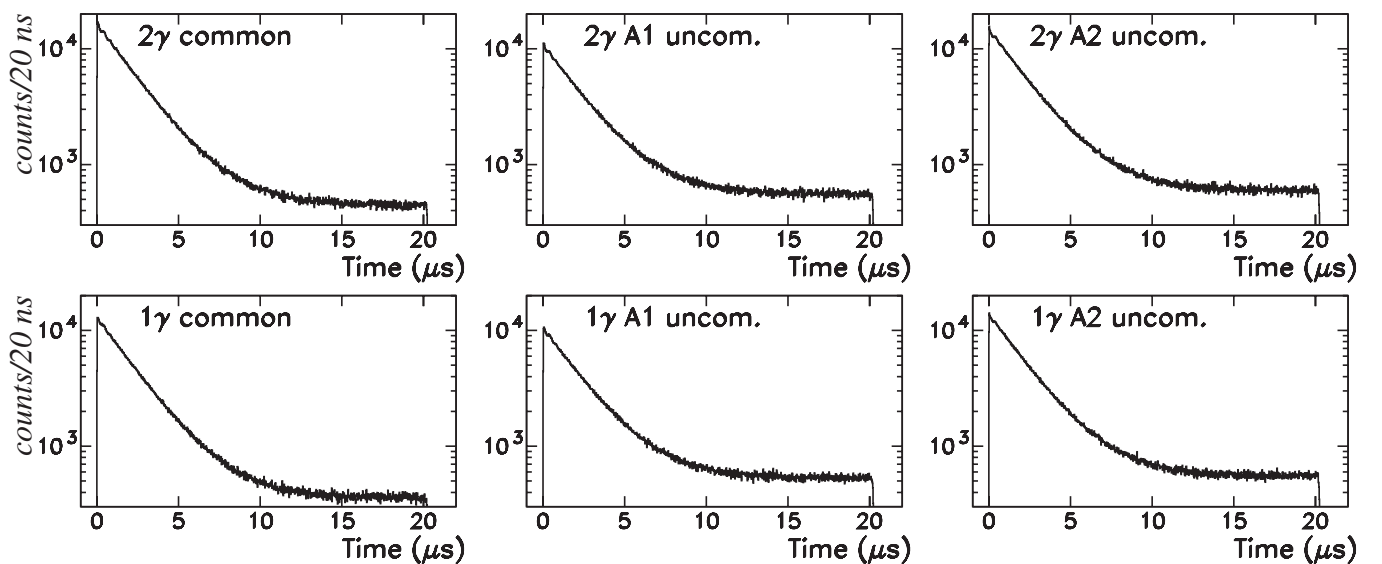

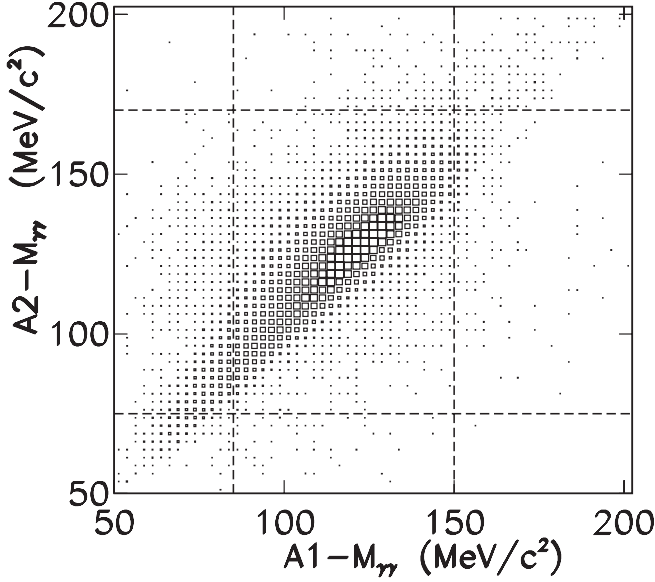FIG. 20. Positron time spectra for 6 data sets of *common*, A1-*uncommon*, and A2-*uncommon* for 2γ and 1γ events

FIG. 21.   Correlation plot of the two photon invariant mass $M_{\gamma\gamma}$ between the A1 and A2 analyses for 2γ events. The selected region in each analysis is indicated with the vertical lines for A1 and horizontal lines for A2.

bwd regions. (There is no mismatch between *fwd* and *bwd* because these regions are separated.)

   (d) Attenuation coefficient $\langle\cos\theta_T\rangle$.—In order to calculate P_T from A_T using the relation Eq. (24) the absolute values of $\langle\cos\theta_T\rangle$ have to be determined individually for each of the data sets. In each analysis $\langle\cos\theta_T^{\mathrm{MC}}\rangle$ had been evaluated by means a Monte Carlo calculation including realistic accidental background conditions. It can be decomposed as the average of

$$\langle\cos\theta_T^{\mathrm{MC}}\rangle = w_c\langle\cos\theta_T^c\rangle + w_u\langle\cos\theta_T^u\rangle, \qquad (35)$$

with statistical weights w_c and w_u which were regarded as being proportional to the number of events in each group, namely, inversely proportional to the squares of δA_N. Because one may assume that $\langle\cos\theta_T^c\rangle/\langle\cos\theta_T^u\rangle =$

TABLE VIII.   Null asymmetry A_0 (in unit 10^{-3}) for the combined data sets for three data periods of I (1996–1997), II (1998), and III (1999–2000).

Data period	I	II	III
= 2γ events =			
A1 · A2 *com* (A1)	-0.41 ± 1.39	-1.95 ± 1.50	-4.71 ± 1.46
A1 · A2 *com* (A2)	-0.41 ± 1.39	-1.92 ± 1.50	-4.67 ± 1.46
A1 *uncommon*	1.91 ± 1.74	-2.96 ± 2.16	-1.34 ± 1.96
A2 *uncommon*	-5.03 ± 1.91	0.02 ± 1.66	-0.65 ± 1.39
= 1γ events =			
A1 · A2 *com* (A1)	-2.03 ± 1.60	-4.28 ± 1.72	-2.19 ± 1.60
A1 · A2 *com* (A2)	-1.98 ± 1.60	-4.39 ± 1.72	-2.12 ± 1.60
A1 *uncommon*	1.62 ± 1.90	-1.04 ± 2.23	-1.74 ± 1.81
A2 *uncommon*	-1.99 ± 1.76	-2.59 ± 1.84	-1.00 ± 1.48

TABLE IX.   Normal asymmetry A_N (in 10^{-2}) and corrected normal asymmetry A_N' (in 10^{-2}) in parentheses for the combined data sets for three data periods of I (1996–1997), II (1998), and III (1999–2000).

Data period	I	II	III
= 2γ events =			
A1 · A2 *com* (A1)	-7.00 ± 0.14	-6.92 ± 0.15	-6.80 ± 0.15
	(-21.1 ± 0.4)	(-20.8 ± 0.5)	(-20.3 ± 0.4)
A1 · A2 *com* (A2)	-6.64 ± 0.14	-6.81 ± 0.15	-6.73 ± 0.15
	(-18.8 ± 0.4)	(-19.6 ± 0.4)	(-19.3 ± 0.4)
A1 *uncommon*	-6.59 ± 0.16	-6.13 ± 0.22	-6.17 ± 0.20
	(-18.9 ± 0.5)	(-17.0 ± 0.6)	(-17.1 ± 0.4)
A2 *uncommon*	-6.58 ± 0.18	-6.20 ± 0.17	-6.09 ± 0.14
	(-17.3 ± 0.5)	(-16.8 ± 0.5)	(-16.6 ± 0.4)
= 1γ events =			
A1 · A2 *com* (A1)	-3.96 ± 0.16	-4.59 ± 0.17	-4.27 ± 0.16
	(-12.6 ± 0.5)	(-14.6 ± 0.6)	(-16.2 ± 0.5)
A1 · A2 *com* (A2)	-3.83 ± 0.16	-4.48 ± 0.17	-4.29 ± 0.16
	(-12.3 ± 0.5)	(-14.5 ± 0.6)	(-15.9 ± 0.5)
A1 *uncommon*	3.75 ± 0.19	-4.24 ± 0.22	-4.29 ± 0.18
	(-12.0 ± 0.6)	(-13.6 ± 0.7)	(-15.6 ± 0.4)
A2 *uncommon*	-3.43 ± 0.18	-3.55 ± 0.18	-4.29 ± 0.15
	(-12.3 ± 0.6)	(-12.5 ± 0.7)	(-15.3 ± 0.6)

$A_N'(\mathrm{com})/A_N'(\mathrm{unc})$, $\langle\cos\theta_T\rangle$s were calculated using the experimentally deduced ratios of $\frac{\langle\cos\theta_T\rangle}{\langle\cos\theta_N\rangle}$ for common and uncommon events. These values are also summarized in Table X. For the common data an average value of A1 and A2 was adopted.

   (e) Decay-plane rotation.—The distributions of θ_r and θ_z are plotted in Figs. 22–24. They are all symmetric about $\theta_{r,z} = 0$ and no singular structure is seen. The θ_r distribution for 1γ events has a structure of two peaks reflecting the presence of the muon holes. This is not the case for the 2γ events where the π^0 has no strong correlation to the muon hole directions. The average values of the decay-plane rotations $\langle\theta_r\rangle$ and $\langle\theta_z\rangle$ are tabulated in Table XI in terms of the relevant quantities [Eq. (27)] for all of the data

TABLE X.   Attenuation factor $\langle\cos\theta_T\rangle$ for the combined data sets for three data periods of I (1996–1997), II (1998), and III (1999–-2000).

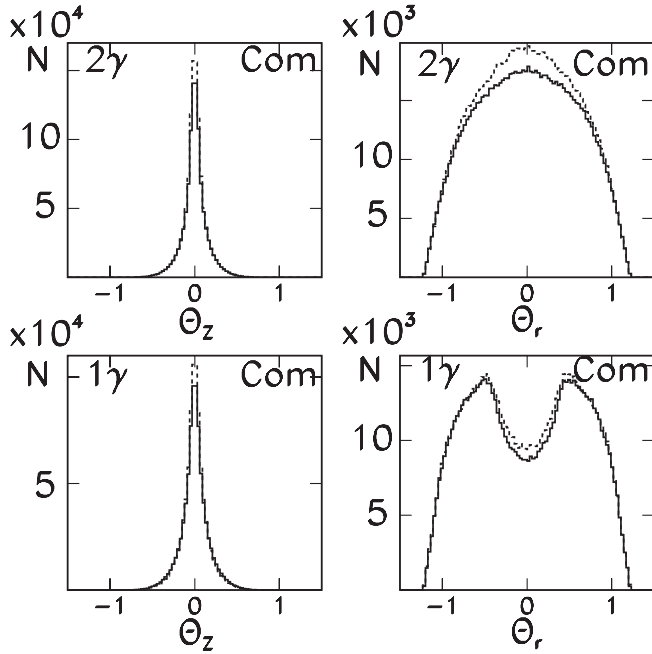| Data period	I	II	III
= 2γ events =			
A1 · A2 *com* (A1)	0.804	0.782	0.767
A1 · A2 *com* (A2)	0.792	0.822	0.822
A1 *uncommon*	0.720	0.638	0.645
A2 *uncommon*	0.729	0.703	0.708
= 1γ events =			
A1 · A2 *com* (A1)	0.646	0.585	0.557
A1 · A2 *com* (A2)	0.649	0.623	0.594
A1 *uncommon*	0.615	0.543	0.589
A2 *uncommon*	0.649	0.537	0.585

FIG. 22. Distribution of decay planes relative to the polarimeter axis for the *common* data. The solid lines are for *fwd* and the dotted lines are for *bwd*.
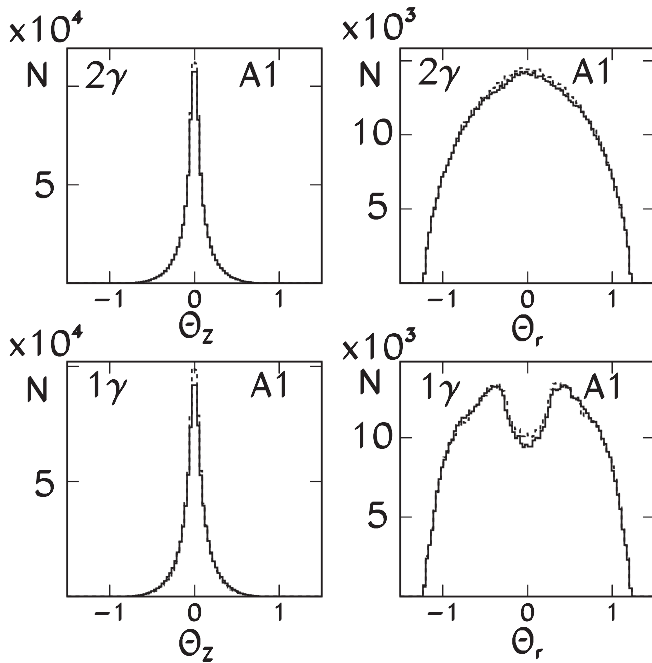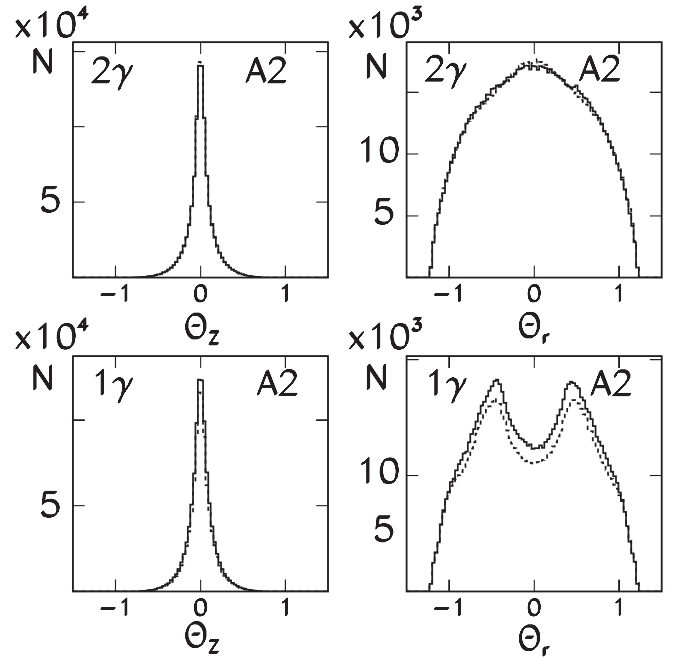

FIG. 24. Distribution of decay planes relative to the polarimeter axis for the A2-*uncommon* data. The solid lines are for *fwd* and the dotted lines are for *bwd*.

sets. They are mostly consistent with zero. There is no degradation observed for the uncommon data sets compared with the common data sets.

(f) Adoption of all the data sets.—From these checks of A_0, A_N, and the decay-plane rotations, it was concluded

that all the data sets were good enough to be included in the final P_T analysis. The decay-plane rotations effect could, in principle, be corrected for, but it was included in the systematic errors.

V. POLARIMETER ANALYSIS AND RESULTS

A. Differential method

1. Asymmetry in the integral analysis

(a) Combined P_T.—One method to extract P_T from the selected data is to use the *cw-ccw* asymmetry of the total e^+ emission in the *fwd/bwd* pion directions. The same quantity of total numbers N_{cw} and N_{ccw} used to calculate A_0 in the individual analyses give the asymmetry $A = (N_{ccw} - N_{cw})/(N_{ccw} + N_{cw})$ for *fwd/bwd*. After the two-analysis combination, $6P_T$s $(i = 1, 6)$ for each run period could be calculated using $\langle \cos\theta_T \rangle^i$ and the analyzing power α as

$$P_T^i = \frac{A_T^i}{\alpha \langle \cos\theta_T \rangle^i}. \tag{36}$$

The first result, employing this method for the data set I was published [57]. The values of A_T^i using the same analysis method for II and III are all consistent with zero and the average result is $A_T^{\text{ave}} = (-0.43 \pm 0.49) \times 10^{-3}$ or $P_T^{\text{ave}} = (-0.22 \pm 0.22) \times 10^{-3}$ with $\chi^2/\text{dof} = 1.30$ and 1.31, respectively. This method, however, suffers from a potential systematic error described in the following section. Therefore, a more exact treatment was developed later and this new method was applied to all the data.

FIG. 23. Distribution of decay planes relative to the polarimeter axis for the A1-*uncommon* data. The solid lines are for *fwd* and the dotted lines are for *bwd*.

TABLE XI. Decay-plane rotations (in mr) for the combined data sets for the three data periods of I (1996–1997), II (1998), and III (1999–2000).

| Data set	$\frac{\langle\theta_z^f\rangle+\langle\theta_z^b\rangle}{2}$ (mr)	$\frac{\langle\theta_r^f\rangle-\langle\theta_r^b\rangle}{2}$ (mr)
I-2γ events		
A1 · A2 *com* (A1)	0.43 ± 0.16	-0.91 ± 0.64
A1 · A2 *com* (A2)	0.33 ± 0.15	-0.73 ± 0.65
A1 *uncommon*	-0.04 ± 0.19	-0.55 ± 0.70
A2 *uncommon*	1.40 ± 0.78	-0.01 ± 0.19
I-1γ events		
A1 · A2 *com* (A1)	0.11 ± 0.21	1.29 ± 0.82
A1 · A2 *com* (A2)	0.17 ± 0.19	1.18 ± 0.82
A1 *uncommon*	0.14 ± 0.22	-0.83 ± 0.81
A2 *uncommon*	0.10 ± 0.18	-0.30 ± 0.76
II-2γ events		
A1 · A2 *com* (A1)	0.19 ± 0.16	0.73 ± 0.65
A1 · A2 *com* (A2)	0.19 ± 0.16	0.59 ± 0.64
A1 *uncommon*	0.07 ± 0.23	0.23 ± 0.84
A2 *uncommon*	-0.27 ± 0.19	0.06 ± 0.73
II-1γ events		
A1 · A2 *com* (A1)	0.07 ± 0.20	-0.05 ± 0.82
A1 · A2 *com* (A2)	0.06 ± 0.20	-0.12 ± 0.82
A1 *uncommon*	-0.11 ± 0.25	1.01 ± 0.92
A2 *uncommon*	-0.10 ± 0.21	-0.16 ± 0.82
III-2γ events		
A1 · A2 *com* (A1)	0.10 ± 0.22	0.39 ± 0.27
A1 · A2 *com* (A2)	-0.01 ± 0.21	0.44 ± 0.27
A1 *uncommon*	0.00 ± 0.26	0.17 ± 0.33
A2 *uncommon*	-0.12 ± 0.22	0.21 ± 0.26
III-1γ events		
A1 · A2 *com* (A1)	0.29 ± 0.26	0.01 ± 0.31
A1 · A2 *com* (A2)	0.33 ± 0.26	-0.05 ± 0.31
A1 *uncommon*	-0.40 ± 0.25	-0.01 ± 0.34
A2 *uncommon*	0.03 ± 0.23	0.10 ± 0.27
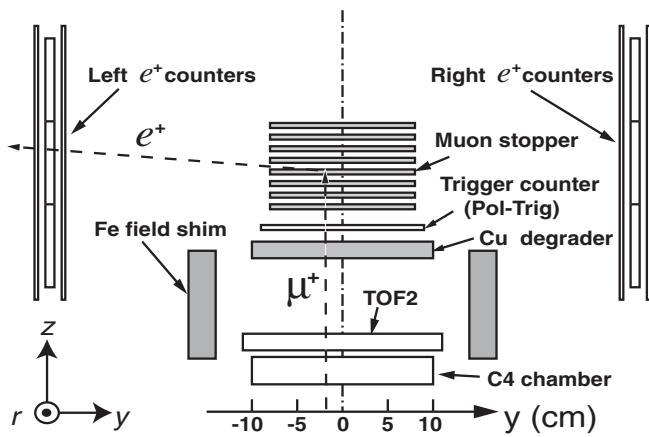
FIG. 25. Cross section of the muon polarimeter of one sector at certain radial position r with the tilted positron counters. The y coordinate was measured by the C4 chamber.

(b) Inherent systematics.—The need for reasonable event rate necessitated the finite size of the muon stopper (Fig. 25). However, the distribution of muon stopping affected the asymmetry very strongly. In particular, a shift along the y direction was critical. Figure 13 shows the asymmetry $A_0(y)$ for the muons at position y. The effect of the shift on the asymmetry is $\delta A = k \times \delta\langle y\rangle$ with $k = 0.015/\text{mm}$ for the average shift $\delta\langle y\rangle$. The A_T measurement relies on the same y distributions between *fwd* and *bwd*, which was not guaranteed, in general, because the decay kinematics were not exactly identical. In fact, a significant $\delta\langle y\rangle$ between *fwd* and *bwd* was observed in the 1γ data in II.

2. Stopping position dependence of A_T and P_T

Such a spurious effect can, in principle, be corrected for by measuring $\langle y\rangle$, but a different approach was adopted to analyze the asymmetry differentially using the y information from the C4 chamber in front of the polarimeter to eliminate this systematic *a priori*. The y dependent T-violating asymmetry $A_T(y)$ was calculated as

$$A_T(y) = \tfrac{1}{2}(A^{fwd}(y) - A^{bwd}(y)), \tag{37}$$

with the y-dependent *fwd* and *bwd* asymmetries

$$A_{fwd}(y) = \frac{1}{2}\left[\frac{N_{cw}^{fwd}(y)}{N_{ccw}^{fwd}(y)} - 1\right] \tag{38a}$$

$$A_{bwd}(y) = \frac{1}{2}\left[\frac{N_{cw}^{bwd}(y)}{N_{ccw}^{bwd}(y)} - 1\right]. \tag{38b}$$

Here, $N_{cw}(y)$ and $N_{ccw}(y)$ are the event number distributions from C4-y. The T-violating polarization at y is then extracted using the relevant analyzing power function of $\alpha(y)$ as

$$P_T(y) = \frac{A_T(y)}{\alpha(y)\langle\cos\theta_T\rangle}. \tag{39}$$

The attenuation factor $\langle\cos\theta_T\rangle$ is independent of y and the values of Table X could be used. This scheme corresponds to the case in which a number of sliced muon stoppers were inserted and the polarization measurements were done for each stopper. The final P_T result for one data set was obtained as the statistical average of $P_T(y)$ as

$$P_T \equiv \langle P_T\rangle = \int P_T(y)w(y)dy, \tag{40}$$

with the normalized weight function of $w(y) \sim 1/\sigma_{P_T}^2(y)$. This microscopic treatment is more exact than the integral method when $\alpha(y)$ is correctly evaluated. Thus, P_T was unaffected by the muon stopping distribution in the stopper.

B. Analyzing power and result

1. Experimental determination of α

(a) Factors affecting the asymmetry coefficient.—There are several factors contributing to the analyzing power α. The polarization independent asymmetry, which is essentially $A_0(y)$, includes the difference in the positron detection solid angle, the effect of positron scattering, and absorption through the stopper material. On the other hand, the polarization dependent asymmetry, which is relevant in the present analysis, involves the intrinsic decay asymmetry and the consequences of muon spin rotation in the magnetic field. In order to extract $\alpha(y)$ the normal asymmetry $A_N(y)$ was used as

$$\alpha(y) = \frac{A_N(y)}{P_N}, \tag{41}$$

with the average of the in-plane polarization of P_N which could be estimated in a Monte Carlo calculation and is independent of y. The normal asymmetry function $A_N(y)$ was deduced as $A_N(y) = (A^L(y) - A^R(y))/2$ with similar definitions of $A^L(y) = (N_{cw}^L(y)/N_{ccw}^L(y) - 1)/2$ and $A^R(y) = (N_{cw}^R(y)/N_{ccw}^R(y) - 1)/2$. In the presence of spin precession in the magnetic field, this $\alpha(y)$ of Eq. (41) is valid only approximately. However, its validity was carefully checked and shown to be good enough for the present analysis.

(b) $\alpha(y)$ function.—Thus, the functional dependence of $\alpha(y)$ could be reduced to that of A_N and determined experimentally. Since $\alpha(y)$ is an intrinsic property of the polarimeter, free from any beam condition dependence or kaon decay kinematics, all the available A_N from all the runs were used to extract a high-statistics $A_N(y)$ up to an absolute value calibration. Furthermore, α should be a symmetric function of y even in the presence of a magnetic
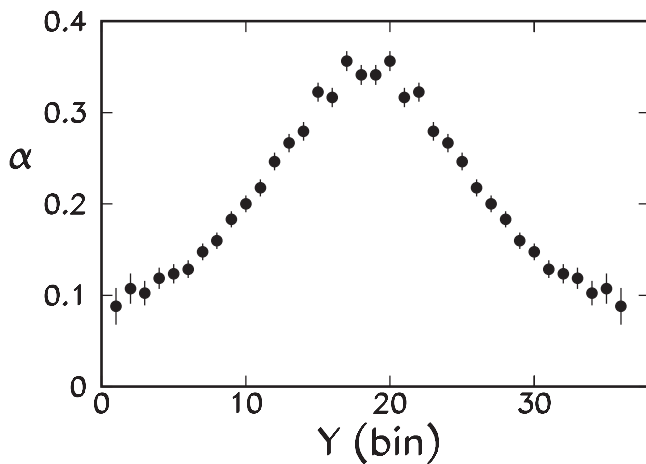

FIG. 26.   Analyzing power function $\alpha(y)$ deduced from $A_N(y)$ of all the data. It was absolutely calibrated. The center of the stopper is at $y = 18.5$. The sides of $y \leq 18$ and $y \geq 19$ were symmetrized.

field. $A_N(y)$ was symmetrized to be an even function as shown in Fig. 26. The analyzing power is maximum at the center and decreases toward both sides of the stopper.

2. Absolute value calibration

In order to determine the absolute value of α the value of P_N was needed. This quantity is governed by the kaon decay phenomenology, in particular, by the real part of the form factor ratio Reξ which still has a large uncertainty. Hence, α was calculated as the ratio of asymmetry to polarization in the Monte Carlo study, namely

$$\alpha_0 = \frac{A_N^{\text{MC}}}{P_N^{\text{MC}}}, \tag{42}$$

where P_N^{MC} is the average polarization calculated in the Monte Carlo calculation providing a realistic muon stopping distribution, and the A_N^{MC} is the integral asymmetry also evaluated realistically taking into account the presence of the magnetic field. By adopting the value $\alpha_0 = 0.270 \pm 0.020$, the absolute scale of $\alpha(y)$ was determined through a relationship obtained also in the Monte Carlo study.

3. P_T results

$A_T(y)$'s are shown in Fig. 27 together with the $A_N(y)$'s. They are nearly flat and consistent with zero. Using the $\alpha(y)$ function, $P_T(y)$ was extracted for all the data sets. The P_T's obtained according to Eq. (40) are summarized in Table XII. There is no significant deviation from zero and all the values are statistically consistent with each other. The standard deviation with $17(= 3 \times 6 - 1)$ degrees of freedom is $\chi^2/\text{dof} = 0.69$ for 2γ and 1.97 for 1γ, respectively. Although the 1γ data is inferior to 2γ all the data sets were accepted giving a final average value of

$$P_T = -0.0017 \pm 0.0023. \tag{43}$$

It is noteworthy that this is almost identical to the result from the integral analysis, $P_T = -0.0018 \pm 0.0023$. The y dependence of the total P_T is plotted in Fig. 28 for 2γ and 1γ separately. There is a small gradient seen both for 2γ and 1γ; this is discussed below.

(a) Origin of y dependence of P_T.—If the $P_T(y)$ of the 18 data sets are examined carefully, gradients are observed in several cases and in the total average. Since there is no systematic tendency of their sign or gradient size, it could be concluded that it originated not from intrinsic reasons like $\alpha(y)$ but from the incident muon kinematics and stopping distribution which were slightly changing from run to run. The intrinsic asymmetry A_0 depends not only on y but also on the radial position r and the stopping depth z through the change in the e^+ counter solid angle. Thus, a slight shift of the muon stopping distribution between *fwd* and *bwd* events in the directions of x and z may lead to a P_T gradient. In the present analysis only the y dependence of A_T was studied, firstly because this dependence is much
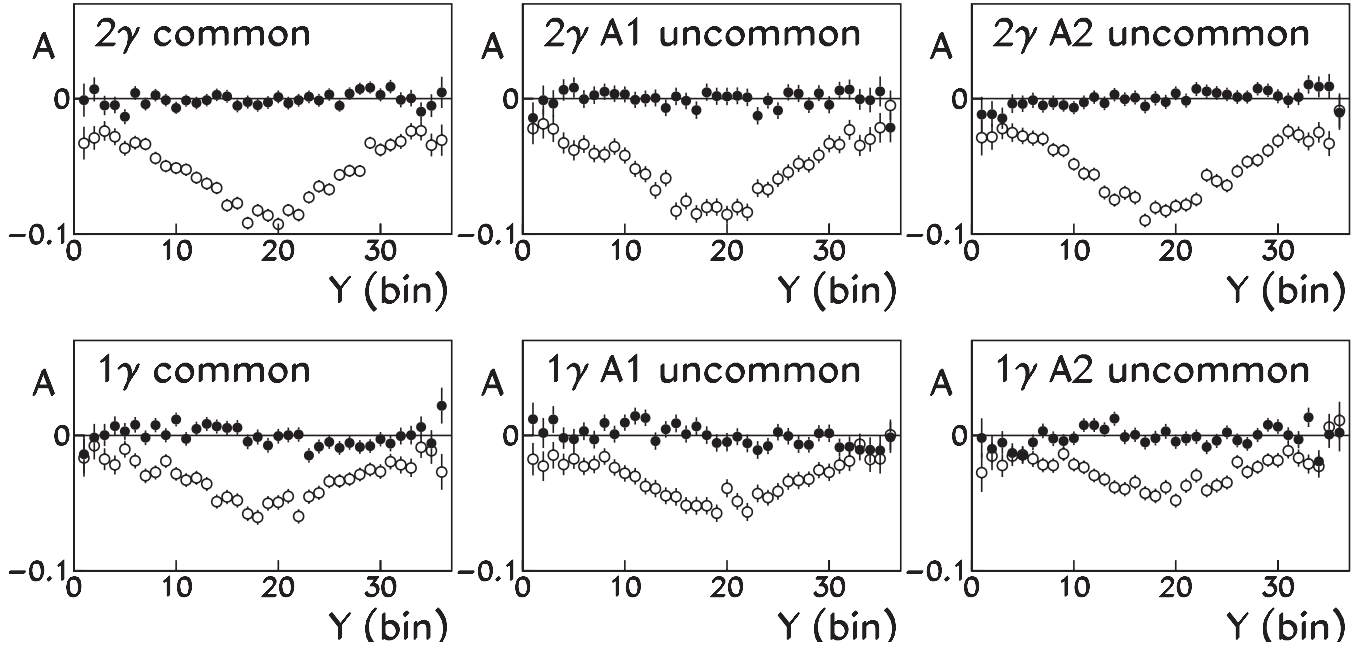
FIG. 27. A_T dependence on C4-y (black dots) plotted together with A_N (open circles) for the 6 data sets

larger (by a factor of 10), and secondly because the stopping point coordinates r and z could only be poorly determined from chamber information relying on a Monte Carlo calculation. These effects due to r and z distribution shifts are fortunately odd functions of y. Therefore, the average value of $P_T(y)$ provides the correct value of P_T if the y projection is symmetric about $y = 0$. The average value of y could be calculated with the weight of $w(y) \sim 1/\sigma_{P_T}{}^2$ as

$$\langle y_{P_T} \rangle = \int_{-9\,\mathrm{cm}}^{+9\,\mathrm{cm}} y w(y) dy. \qquad (44)$$

This is small—$\langle y_{P_T} \rangle = (0.007 \pm 0.016)$ mm for 2γ and (0.020 ± 0.017) mm for 1γ, respectively, confirming the validity of the present analysis.

C. Deduction of Imξ

Conversion factor $\langle P_T/\mathrm{Im}\xi \rangle$

Since the asymmetry A_T is dependent on the polarization P_T distribution in the stopper and it is determined by Imξ

as well as by Reξ, it can be calculated from the relation between A_T and these parameters. However, in the present analysis an approximate procedure of two steps was chosen using the average $\langle P_T \rangle$. Namely, the factorization was assumed as

$$A_T = \langle A_T/\mathrm{Im}\xi \rangle \, \mathrm{Im}\xi \sim \alpha \langle P_T \rangle \langle \cos\theta_T \rangle$$
$$= \alpha \langle P_T/\mathrm{Im}\xi \rangle \langle \cos\theta_T \rangle \, \mathrm{Im}\xi, \qquad (45)$$

and all the beam and background dependent effects are included in the term $\langle \cos\theta_T \rangle$ leaving $\Phi = \langle P_T/\mathrm{Im}\xi \rangle$ as a constant determined only by detector geometry. This was calculated in a Monte Carlo simulation assuming Re$\xi = 0.35$ to be $\Phi = 0.327$ and 0.287 for 2γ and 1γ, respectively. Further, it was confirmed that this approximation using the average $\langle P_T \rangle$ of the stopped muon is good within several percent error. Following this formulation Imξ was extracted as

$$\mathrm{Im}\,\xi = \frac{\langle P_T \rangle}{\Phi}, \qquad (46)$$

TABLE XII.   *T*-violating polarization P_T of the 18 data sets of 2γ and 1γ events from the two analyses of A1 and A2 for the three experimental periods. The errors are statistical only. For the definitions of event categories, see the text.

| Data category	I (1996–1997)	II (1998)	III (1999–2000)
2γ[A1 · A2]	0.001 12 ± 0.006 67	−0.003 17 ± 0.007 29	−0.005 96 ± 0.007 11
2γ[A1bar · A2]	−0.007 35 ± 0.010 22	0.012 25 ± 0.008 58	−0.000 37 ± 0.007 54
2γ[A1 · A2bar]	−0.003 85 ± 0.008 99	0.006 40 ± 0.012 68	−0.004 73 ± 0.012 01
1γ[A1 · A2]	−0.013 93 ± 0.009 56	−0.013 66 ± 0.010 42	0.011 13 ± 0.010 35
1γ[A1bar · A2]	0.010 14 ± 0.010 69	−0.011 14 ± 0.012 80	−0.010 88 ± 0.010 22
1γ[A1 · A2bar]	0.002 28 ± 0.011 34	−0.016 60 ± 0.015 31	0.009 51 ± 0.011 95
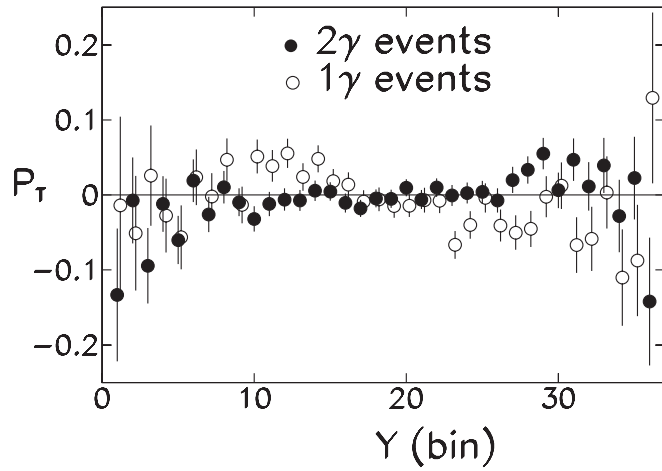
FIG. 28. P_T dependence on C4-y. Black dots are 2γ events and open circles are 1γ events. The center of the stopper is at $y = 18.5$.

and Im$\xi = -0.0053 \pm 0.0071$ was obtained. The statistical error of Φ was negligibly small and the error due to this approximation is also small. Figure 29 shows the statistical scattering of these results and the good behavior of the ideogram.

D. P_T dependence on variables

Only the average P_T has been analyzed and discussed in the present work although a differential analysis in terms of pion energy E_{π^0} and muon energy E_{μ^+} should eventually be possible with the consequence of better sensitivity to Imξ. Unfortunately, the present number of events was not
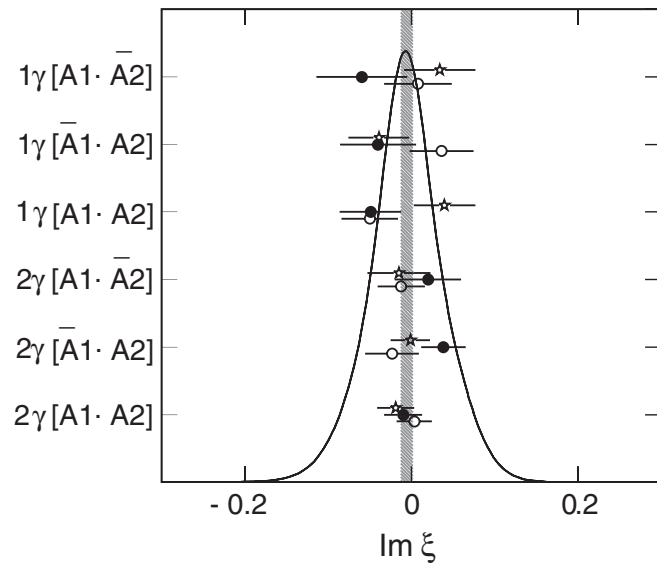

FIG. 29.   Ideogram of Imξ for the 18 data sets. A statistical distribution with $\chi^2/\text{dof} = 0.78$ is observed. The black dots are for data set I, the open circles are for II, and the stars are for III. The hatched stripe indicates Im$\xi = -0.0053 \pm 0.0071$.

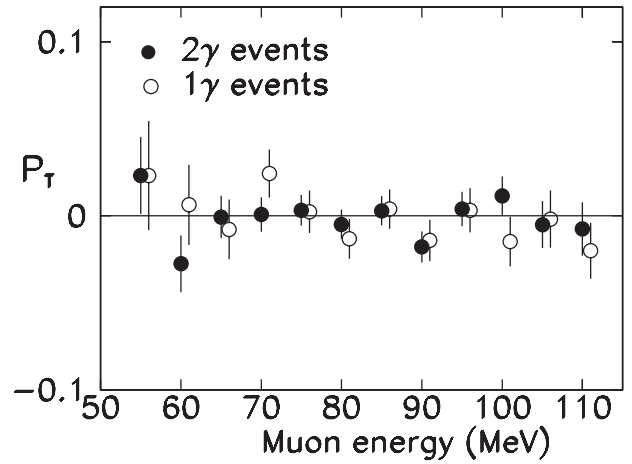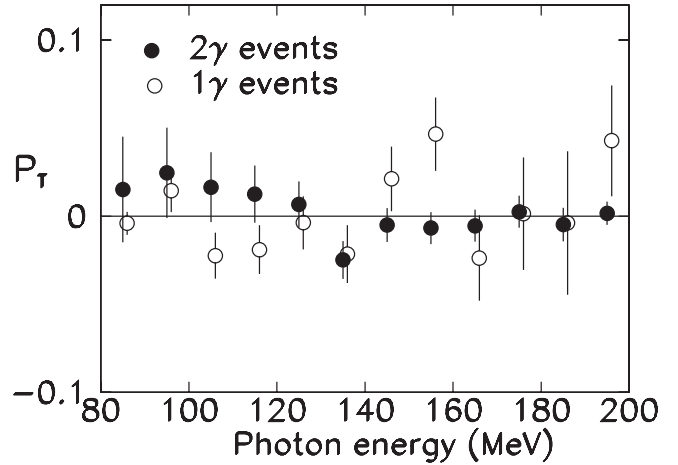FIG. 30. P_T dependence on muon energy for 2γ and 1γ events.

FIG. 31. P_T dependence on photon energy. For 2γ events the sum energy (namely, the π^0 energy) was taken. For 1γ events the energy of the observed photon was taken.
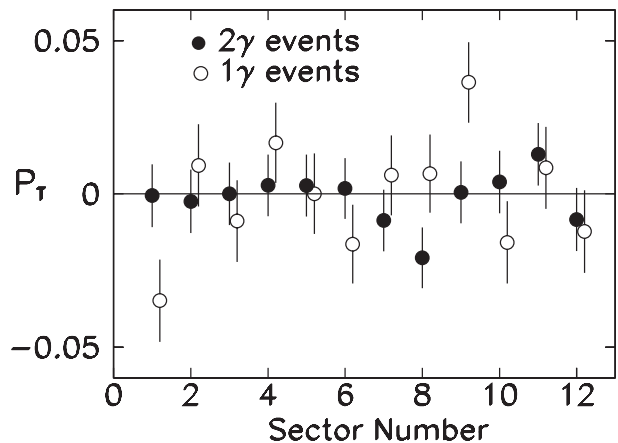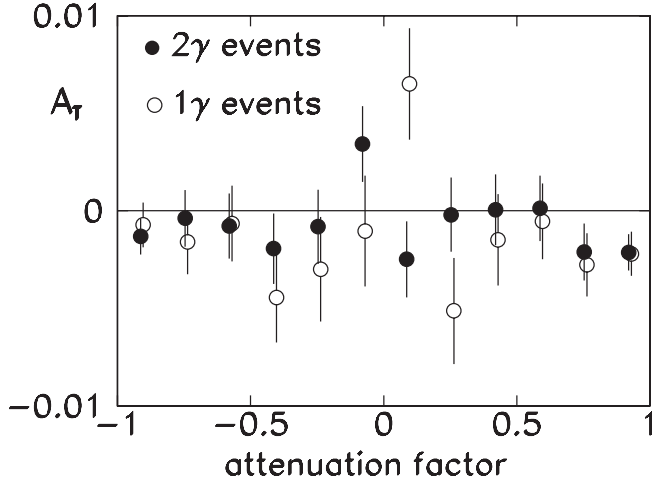

FIG. 32. P_T of each gap.

FIG. 33. A_T dependence on the average of the attenuation factor which is defined by Eq. (19) and is nearly the cosine of the π^0 polar angle $\theta_{\pi^0(\gamma)}$. The final result of the present experiment corresponds to the ratio between the regions of >0.342 and < -0.342.

large enough for such analyses. However, it was important to check the P_T dependence on these variables to see that no strange behavior appeared. Figure 30 shows the E_{μ^+} dependence. As was shown in Fig. 1 P_T should be predominant for higher E_{μ^+} if Imξ is nonzero, but there is no such tendency seen here either for 2γ or 1γ. Figure 31 is a similar plot for the photon energy. There is no strange behavior or tendency seen for either 2γ or 1γ. Finally, an overall systematic could be checked using the P_T values in the 12 sectors as shown in Fig. 32. The χ^2/dof values are 0.69 and 1.97 for 2γ and 1γ, respectively, with inferior data quality for 1γ. The A_T dependence on the attenuation factor [Eq. (11)] is shown in Fig. 33.

VI. SYSTEMATIC ERRORS

A. Origins of spurious effects

All possible sources of spurious effects which may mimic P_T were thoroughly investigated and verified to be small. They were treated as systematic errors rather than corrections for their estimated spurious δP_T^{sp}, because the size of δP_T^{sp} turned out to be smaller than the current statistical error and the estimates of δP_T^{sp} themselves involved certain uncertainties. There were also systematic errors which added some ambiguities (rather than a spurious P_T bias) to the obtained value of P_T such as the error associated with the analysis. However, their contributions were much smaller.

δP_T^{sp} could be induced by the admixture of a large in-plane component of P_L or P_N or some systematics effects which gave a bias to A_T, due to instrumental or experimental conditions. The conceivable sources can be categorized

into three groups: (i) geometrical misalignments of detector elements resulting in distortion of the decay-plane distribution relative to the polarimeter axes, (ii) asymmetries of events in the decay kinematic phase space, and (iii) spurious A_T in the polarimeter due to geometrical and analysis reasons. They are related to each other to some extent and they are sometimes difficult to separate. However, it was assumed in the error analysis that all the sources contributed independently, to be added quadratically at the end. They were, strictly speaking, also related to the cut conditions in the event selection and dependent on the final data sets, but the error estimates were done for a typical data set and applied for all the final data sets.

In the following the possible systematic errors (listed as $a \sim n$) are estimated item-by-item in order to obtain the value of the total systematic error.

B. Misalignments of detector elements

The geometrical reference frame of the experiment was the polarimeter axis which had been installed with high precision relative to the relevant magnet gap. The rotational symmetry of the 12 sectors was also sufficiently high (roughly speaking 2 mm alignment across the global size of the magnet of 4 m corresponding to 10^{-3} precision). The CsI(Tl) barrel unit was also assembled with high precision [52]. The most dangerous systematics were from the accuracy of the alignments of (a) the CsI(Tl) barrel unit relative to the magnet, and (b) the misalignments of the MWPC chambers.

(a) CsI(Tl) barrel alignment.—The effects of a global rotation of the CsI(Tl) unit about the x and y axes are expected to cancel after summation over the 12 gaps. More importantly this does not induce a net rotation of the decay-plane distribution about the z axis. Indeed, a Monte Carlo simulation taking into account a realistic accuracy of 10 mr resulted in a maximum asymmetry of 6×10^{-4} which was suppressed further by taking the *fwd* and *bwd* difference. Thus, it was harmless. However, a rotation about the z axis, namely, the beam axis, results in a finite effect even after the 12 gap summation. Another Monte Carlo simulation assuming a potential value of 15 mr for the azimuthal accuracy determined 1.6×10^{-4} for δP_T^{sp} after a *fwd-bwd* subtraction.

(b) MWPC alignment.—The shifts of the MWPC chambers C2, C3, and C4 also affect the distribution of the decay plane. Here, only the azimuthal offsets are relevant and the shifts in the r and z directions have no effect in first order. The possible rotation of the decay plane could be inferred to be about 0.4 mr from the change when the fiducial volume in terms of C4-y was varied. This value corresponds to a C4 shift of about 0.7 mm when only the C4 position was assumed to be responsible. This value was consistent with the actual position measurement of the y alignment of C4 after the detector completion implying

rather better alignment for the upstream chamber, C2. The alignment of C2 at the installation was done aiming for 0.2 mm but no measurement was possible after the completion of the setup. A rotation of 0.4 mr corresponds to $\delta P_T^{\text{sp}} = 2.0 \times 10^{-4}$.

C. Asymmetry in decay phase space

Since the measurement assumes a symmetric distribution of decay planes relative to the magnet-gap median planes, its distribution had to be checked. Even though the detector was geometrically symmetric there were a few factors which had the potential for such asymmetries: (i) the chamber inefficiency distribution, (ii) the asymmetry in the initial kaon stopping distribution in the target, and (iii) some cut conditions in the analysis which might have resulted in an asymmetry.

(c) Detector inefficiencies.—During the measurement all the tracking element channels of the MWPC and the target/ring counters were operational with very high and uniform sensitivities. Although the high voltage of some of the chambers tripped occasionally, it was soon recovered and the net down-time was negligibly small. There were no conceivable correlations between the inefficiency distribution (or dead-time of any chamber) and the decay-plane distributions. These effects, even if significant, were *fwd-bwd* canceling. Two modules of the CsI(Tl) barrel went dead soon after the start of the measurement and were never fixed.

(d) Kaon stopping distributions.—As was shown in Fig. 6, the kaon stopping distribution was tilted in the horizontal plane due to the nonzero beam momentum dispersion resulting in different stopping depths. The *C*4-*y* distribution in the vertical gaps has a large shift because the acceptance for the front and rear parts of the target was quite different, and accordingly the null asymmetry, A_0, has a sinusoidal dependence with an amplitude of nearly 2×10^{-3}. However, these values were canceled by the summation over 12 gaps. With regard to the *fwd-bwd* cancellation, this does not work perfectly because of the preference of the front (back) part of the target for *fwd(bwd)* events due to solid angle and absorption. Although this kaon distribution effect could be checked by the decay-plane rotation, it was independently estimated to give an expected upper bound $\delta P_T < 3 \times 10^{-4}$ using the data.

(e) Overall test by decay-plane rotation.—The relevant distortion of the decay phase space including the above mentioned effects could be checked in overall form in terms of the decay-plane distribution, and, in the present case, by its average values since the effect is linear. The values of Table XI for $(\langle \theta_z^f \rangle + \langle \theta_z^b \rangle)/2$ and $(\langle \theta_r^f \rangle - \langle \theta_r^b \rangle)/2$ yield average value *one-σ* upper bounds of 2.40×10^{-4} and 1.32×10^{-4}, respectively. By assuming 0.5 for both P_N and P_L from Monte Carlo simulation, $\delta P_T^{\text{sp}} = 1.2 \times 10^{-4}$ and 6.6×10^{-5} could be obtained from Eq. (27). It is

noted that none of the cancellation mechanisms was effective for the former.

D. Errors in polarization measurement

In the polarimeter, there are several systematics which not only give a bias to the asymmetry but also admix P_N and P_L. To the former belong the misalignments of the positron counters and other detector elements, and to the latter belongs the asymmetry of the magnetic fields on the muon stoppers. The effect of muon multiple scattering through the copper degrader, although it does not give a bias, produces an ambiguity in A_T. The finite size of the muon stopping distribution required a differential analysis, but the lack of r and z information leaves an uncertainty in the final P_T when extracted by integrating over y.

(f) Positron counter misalignments.—Five kinds of misalignments were considered: three offsets in ϕ, r, and z directions and rotations about r and z axes for a single individual counter. By using a Monte Carlo simulation the conversion coefficients (A_T/offset) were estimated for each misalignment. As was easily imagined the offsets in the azimuthal ϕ direction had a major effect. These offsets were assumed to be the values which were measured once during the run in 1997 and then after the run in 2002 with different reference points. The conversion coefficient was estimated conservatively to be $2.5 \times 10^{-3}/$ mm taking into account the possible uncertainty during the two measurements. The estimated δP_T^{sp} was 2.4×10^{-4}. In order to estimate δP_T from other sources, the maximum setting tolerance at the mounting was used, but the estimated values were 1 order of magnitude smaller as seen in Table XIII. Misalignments of other components, the muon stopper position, and the Pol-trig counter position were also investigated by a Monte Carlo simulation with conceivable maximum offsets. However, their effects were also found to be small.

(g) Magnetic field misalignments.—The symmetric distribution of the field was essential to avoid an overall admixture of the in-plane polarization components due to precession when integrated over the muon stopping distribution. The asymmetry of the distribution over the relevant volume can be described in terms of three parameters: (i) the offset in the azimuthal direction ϵ, (ii) the rotation about the z-axis, δ_z, and (iii) the rotation about the r-axis, δ_r. The rotation about the y-axis does not give a significant contribution. Their effects were evaluated in a Monte Carlo simulation using a realistic muon distribution as

$$\delta A_T = 4.7 \times 10^{-4} \epsilon \, [\text{mm}] + 7.4 \times 10^{-5} \delta_z + 5.7 \times 10^{-5} \delta_r, \tag{47}$$

where δ_z and δ_r are in units of mr. The 12 field maps were carefully analyzed yielding average values of $\bar{\epsilon} = 0.90$ mm, $\bar{\delta}_z = 0.15$ mr, and $\bar{\delta}_r = 1.6$ mr. By adding

TABLE XIII.   Summary of major systematic errors.

Source	Canceled by Σ_{12}	Canceled by *fwd/bwd*	$\delta P_T \times 10^4$
e^+ counter r-rotation	Yes	Yes	0.5
e^+ counter z-rotation	Yes	Yes	0.2
e^+ counter ϕ-offset	No	Yes	2.8
e^+ counter r-offset	Yes	Yes	<0.1
e^+ counter z-offset	Yes	Yes	<0.1
$\vec{B}$ offset (ϵ)	No	Yes	3.0
$\vec{B}$ rotation (δ_r)	No	Yes	0.37
$\vec{B}$ rotation (δ_z)	No	No	5.3
μ^+ counter y-offset	No	Yes	<0.1
CsI(Tl) misalignment	Yes	Yes	1.6
K^+ stop distribution	Yes	Yes	<3.0
MWPC y-offset (C4)	No	Yes	2.0
K^+ DIF background	Yes	No	<1.9
$K_{\pi 2}$ DIF background	No	Yes	0.6
μ^+ multiple scattering	Yes	No	7.1
e^+ time spectrum	No	Yes	0.8
Decay-plane angle (θ_r)	No	Yes	1.2
Decay-plane angle (θ_z)	No	No	0.66
Uncertainty of α	$\cdots$	$\cdots$	1.3
$\langle \cos\theta_T \rangle$ uncertainty	$\cdots$	$\cdots$	3.3
P_T gradient	$\cdots$	$\cdots$	0.3
Analysis	$\cdots$	$\cdots$	0.9
Total			11.4

the uncertainties of the measurement quadratically, *one-σ* errors were determined to be $\sigma(\epsilon) = 0.92$ mm, $\sigma(\delta_z) = 1.0$ mr, and $\sigma(\delta_r) = 1.9$ mr. Taking into account the *fwd-bwd* cancellation for ϵ and δ_r, $\delta P_T(\epsilon) = 3.0 \times 10^{-4}$, $\delta P_T(\delta_z) = 5.3 \times 10^{-4}$, and $\delta P_T(\delta_r) = 3.7 \times 10^{-5}$ were obtained. It is noted here that there is no cancellation working for δ_z just as in the case of $\langle \theta_z \rangle$.

(h) Muon multiple scattering.—The muon suffers from multiple scattering while passing through the thick Cu degrader. Since the differential analysis was based on the y coordinate measured by the C4 chamber, this scattering effect had to be taken into account. Namely, the real muon stopping distribution of $y^{\rm real}$ could be statistically fluctuating and the mean geometrical asymmetry, A_0, might be slightly different from that determined by the C4y distribution. This effect is essentially the statistical error which approaches zero as event number increases, but this is treated as a systematic error in the present analysis. The mean value of $y^{\rm real}$ should have a *one-σ* statistical fluctuation as

$$\sigma(\langle y \rangle) = \sigma(y)/\sqrt{N}, \qquad (48)$$

where $\sigma(y)$ is the width of y due to multiple scattering and N is the number of events. From the Monte Carlo simulation $\sigma(y)$ was estimated and the ambiguity of the asymmetry

$$\delta A_T = k \times \sigma(\langle y \rangle) \qquad (49)$$

could be calculated with the gradient k of $A_0(y)$ (Fig. 13), corresponding to the largest error in $\delta P_T = 7.1 \times 10^{-4}$.

(i) P_T gradients.—As was discussed in Sec. V the gradients observed for the y dependence of $P_T(y)$ could be attributed to the nonidentical r or z distributions of the muon stop between *fwd* and *bwd* distributions, which could be canceled out when the y distribution is symmetric across $y = 0$ because of the odd nature of these effects. The weighted mean values of $\langle y_{P_T} \rangle$ [Eq. (44)] can be used as a measure of the systematic error associated with this fact. The errors were estimated by using gradient coefficients h from fitting, $h = (0.31 \pm 0.09) \times 10^{-3}$/mm ($\chi^2$/dof = 0.9) and $h = (-0.63 \pm 0.11) \times 10^{-3}$/mm ($\chi^2$/dof = 1.4), respectively, for 2γ and 1γ. This led to $h\langle y_{P_T} \rangle$ of $(7.1 \pm 2.1) \times 10^{-6}$ and $(-23.3 \pm 4.1) \times 10^{-6}$ taking into account the error of $\langle y_{P_T} \rangle$. In order to be conservative we adopted the value for 1γ as a common value to obtain $\delta P_T = (23.3 + 4.1) \times 10^{-6} = 2.7 \times 10^{-5}$.

E. Background contamination

The accidental background, especially in the Cs(Tl), was not a source of bias in P_T, but the physics backgrounds of $K_{\pi 2}$ decay-in-flight and $K_{\mu 3}$ events from K^+ decay-in-flight were able to produce a spurious P_T and their upper bounds were checked.

(j) $K_{\pi 2}$ pion decay-in-flight.—The $K_{\pi 2}$ decay-in-flight, in particular, a transverse decay, has a muon transverse polarization component, if it is not completely canceled between left-hand side decay and right-hand side decay in a gap. This effect was extracted as the asymmetry of the rejected events with bad tracking χ^2 (A2) or bad hit/fit difference of the target/ring with $\theta_{\pi\mu} > 160°(2\gamma)$, $150°(1\gamma)$ (A1). In the actual evaluation, the 1γ data of A1 with the most contamination was selected for a conservative estimate. The measured asymmetry $A_{K_{\pi 2}}$, the ratio of fractions, and the *fwd/bwd* cancellation power yielded an upper bound of $\delta P_T = 6 \times 10^{-5}$. The insignificance of this effect was also confirmed in the A_T cut-point dependences on the relevant variables.

(k) Kaon decay-in-flight.—The estimate of the possible polarization from the kaon decay-in-flight contamination relied on a symmetry consideration; the extraction of its effect using the prompt part in the kaon decay time spectrum was statistically insignificant. A screw-sense effect (azimuthal polarization) appears when the incident kaon beam has a tilted momentum $\delta\vec{p}_K$ which is coupled to another offset vector $\delta\vec{r}$, as $\delta P_T \sim \delta\vec{p}_K \times \delta\vec{r}$. Here, $\delta\vec{r}$ can be e.g. a shift of the beam center, but the imbalance of the detector acceptance across the tilt plane is most important. A conservative estimate of the beam tilt of 30 mr (primarily horizontal) and perpendicular detector acceptance imbalance of 25% taking into account the existence of the muon holes, a residual decay-plane tilt of 1.9×10^{-4} could be evaluated, which can be regarded as the degree of the in-plane polarization admixture.

F. Errors associated with analysis

The uncertainties associated with the analysis did not produce biases in P_T, but they decreased the experimental accuracy, and could be treated as a systematic error.

(l) Positron time spectrum analysis.—Since the deduction of the asymmetry A_T is based on the positron yields analyzed from the time spectrum, its ambiguity has a direct influence on P_T. The choice of an extraction method (Sec. IV) turned out not to affect the extracted asymmetry significantly. The most serious uncertainty comes from the validity of the flat constant background assumption, even if the fitting provides a sufficiently good χ^2 value. In fact, the beam spill time structure (when it was not well tuned and had a periodic time structure) could produce a correlated structure in the time spectrum. Although the main parts of the constant background were attributed to accidental "room background" associated with the pion flux in the beam, gap cross-talk events were, in principle, possible. In this case the background may have an exponential component. In order to estimate its influence, the spectra of "not triggered gaps" (empty gaps) were carefully studied using a typical fraction of the data. Indeed, the flatness of the spectrum was confirmed but with a small (3%) exponential component even at the 180° opposite gap. Using these data, it was concluded that the uncertainty of A_T due to this effect was less than 10^{-5} corresponding to δP_T of 8×10^{-5} after fwd/bwd subtraction. The integrated areas of the time spectra are also affected by hardware items such as the calibration of the time origin in the TDCs. However, their contributions was estimated to be less than $\delta P_T = 10^{-5}$.

(m) Error of $\langle\cos\theta_T\rangle$.—In the combined analysis in terms of Eq. (39), the ambiguity of $\langle\cos\theta_T\rangle$ affects the final result. There are two sources for this ambiguity. One is related to the method of estimating $\langle\cos\theta_T\rangle$ for the common and uncommon parts from the total $\langle\cos\theta_T\rangle$ in a Monte Carlo simulation using the information on A_N, $\langle\cos\theta_T\rangle_{\exp}$ and $\langle\cos\theta_N\rangle_{\exp}$ without any background consideration. This concerns the relative ambiguity among 6 $\langle\cos\theta_T\rangle$'s. The second reason is related to the estimate of the absolute values of the $\langle\cos\theta_T\rangle$ estimation in the Monte Carlo calculations. These two factors were estimated to give rise to an ambiguity of 3.5×10^{-4} in total.

(n) Ambiguity of the analyzing power α.—The replacement of the $\alpha(y)$ function by $A_N(y)/P_N$ in Eq. (39) and the further simplification of symmetrization about $y = 0$ was regarded to be justified with 5% accuracy. As long as the error of each point of the analyzing power function (Fig. 26) is statistical, its influence on $\delta P_T(y)$ is negligibly small as seen from the relation

$$\sigma^2_{P_T} = \left(\frac{\sigma_{A_T}}{\alpha}\right)^2 + \left(P_T\frac{\sigma_\alpha}{\alpha}\right)^2 \sim \left(\frac{\sigma_{A_T}}{\alpha}\right)^2. \qquad (50)$$

A systematic bias in the $\alpha(y)$ function and the ambiguity of the absolute value calibration by means of a Monte Carlo calculation can change the central value P_T^c of the average P_T in Eq. (40) as $P_T^c(1 \pm \delta)$. Although there was no systematics observed for the former, a conservative estimate was made by assuming 5% effects for both to obtain $\delta P_T = 1.3 \times 10^{-4}$.

G. Total systematic error

All the systematic errors discussed above are summarized in Table XIII. Some of the δP_T values have no meaning as *one-σ* error but only give the maximum conceivable ranges of values. However, all the items were quadratically added to yield $\delta P_T^{\text{total}} = 1.1 \times 10^{-3}$, which can be regarded as a kind of *one-σ* error. This is compared to the statistical error which is twice as large. By including this total systematic error, the P_T final result is

$$P_T = -0.0017 \pm 0.0023(\text{stat}) \pm 0.0011(\text{syst})$$

$$= -0.0017 \pm 0.0026 \qquad (51)$$

by adding the statistical and systematic errors quadratically.

VII. DISCUSSION

The present result sets an upper limit on Imξ which is a factor three improvement over the BNL-AGS result with K^+ mesons. Our result constrains the exotic scalar coupling G_S in the decay to be $|\text{Im}G_S|/G_F < 2.2 \times 10^{-4}$ assuming $m_s = 100$ MeV according to Eq. (13). This is one of the most stringent constraints on scalar interactions. It is noted that another exotic pseudoscalar coupling can be constrained by P_T in $K_{\mu\nu\gamma}$ decay together with an exotic right-handed interaction [31,63].

For the scalar coupling several models have been investigated. We would like to briefly discuss the impact of our result on each of them. In the three-Higgs-doublet model [34] with natural flavor conservation, which is one of the simplest extensions of SM into the Higgs sector, P_T is connected as $\text{Im}\xi = \text{Im}(\alpha_1\gamma_1^*)(m_K/m_{H_1})^2$ to the product of two coupling constants α_1 and γ_1 of the lighter exchanged Higgs boson to the quark current and the lepton current, respectively. Our result corresponds to a limit of $|\text{Im}(\alpha_1\gamma_1^*)| < 544(M_{H_1}/\text{GeV})^2$, which is more stringent than the limit of $<1900(M_{H_1}/\text{GeV})^2$ from B-meson decay $B \to X\tau\nu$ [64]. For the three-Higgs-doublet model, another strong constraint comes from the neutron electric dipole moment d_n. This is proportional to another parameter $\text{Im}(\alpha_1\beta_1^*)$ with a second coupling to the quarks β_1 constraining the model in a different manner, but with a relation $\text{Im}(\alpha_1\beta_1^*) = (v_2/v_3)^2 \text{Im}(\alpha_1\gamma_1^*)$ using the vacuum expectation values relevant to the Higgs fields v_2 and v_3. Garisto and Kane [35] have derived an interesting connection between P_T and the neutron electric dipole moment (d_n) under the assumption of $R = v_2/v_3 \sim m_t/m_\tau$ (where m_t and m_τ are the top mass and the τ mass, respectively),

viz.,

$$P_T \approx 2.3 \times 10^{-3} \left[\frac{m_t}{130}\right]^2 \left[\frac{0.3}{m_d}\right] d_n^d \times 10^{26}, \quad (52)$$

where m_t and m_d (down quark mass) are in GeV units and d_n^d is the d-quark contribution to the neutron electric dipole moment in units of $e \cdot$ cm. Taking $m_t = 175$ GeV, $m_d = 0.3$ GeV (the constituent mass for a safe estimate), we deduce $d_n^d < 7 \times 10^{-27} e$ cm. Since there may be contributions other than d_n^d, it can be said that P_T is not constrained by d_n any stronger than the present result unless its experimental bound reaches the level of $10^{-26} e$ cm. The $b \to s\gamma$ decay also constraints $\mathrm{Im}(\alpha_1 \beta_1^*)$ [23] but this is less stringent.

Wu and Ng [38] have studied the quark-squark misalignment in SUSY, which in turn leads to flavor changing neutral current processes and acts as a new source of T violation. In this model, P_T with the muon and neutrino directions at right angles, is given as

$$P_T^{H^+} \approx 3.5 \times 10^{-3} I_{H^+} \frac{p_\mu}{E_\mu} \frac{(\mu + A_t \cot\beta)}{m_g} \frac{(100 \text{ GeV})^2}{M_H^2}$$

$$\times \frac{\mathrm{Im}[V_{33}^{H^+} V_{32}^{D_L^*} V_{31}^{U_R^*}]}{\sin\theta_c}, \quad (53)$$

for the generally used value of $\tan\beta \approx 50$. For the meanings of various symbols see Ref. [38] except to note that we assumed the top quark mass to be 180 GeV. Our P_T upper bound corresponds to $M_H > 140$ GeV. In view of the approximations made to arrive at this result, it should be considered as a qualitative estimate [65].

In R-parity violating SUSY [37] the parameters $\mathrm{Im}[\lambda_{2i2}(\lambda_{i12}')^*]/M^2$ and $\mathrm{Im}[\lambda_{21k}'(\lambda_{22k}')^*]/M^2$ are constrained, where the former is for the slepton exchange and the latter is for the down-type squark exchange and M is the mass scale, respectively. For the relevant 4 combinations of $\lambda(\lambda')^*$ and $\lambda'(\lambda')^*$, constraints from other experimental limits are not stringent enough; thus, our P_T result determines their limits as a function of the mass scale M.

In a discussion of the leptoquark model, Garisto and Kane [35] also employed a connection between the rare decays such as $K_L \to \mu e$. They deduced

$$P_T \le 2.6 \times 10^{-3} \left[\frac{R}{72}\right] \left[\frac{BR(K_L \to \mu e)}{2 \times 10^{-10}}\right]^{1/2}. \quad (54)$$

The current upper limit $BR(K_L \to \mu e) < 4.7 \times 10^{-12}$ [66] can be related to $P_T < 5 \times 10^{-4}$ with $R = v_2/v_3 \approx m_t/m_\tau$ indicating a weaker constraining power of P_T for this model.

As a sequel to E246, it is proposed to measure P_T at the J-PARC facility currently under construction in Japan [67]. Our goal is to improve the limit by about a factor of 20—50 from the result reported here. This result would provide knowledge of flavor off-diagonal scalar and tensor interactions which are not accessible in collider experiments and do not appear in other high-precision experiments such as electric dipole moments [68].

VIII. SUMMARY

Experiment E246 at KEK has searched for a transverse muon polarization, P_T, in $K_{\mu3}^+$ decay, which would be a signature of T violation. P_T is a sensitive probe of new physics beyond the SM, since its SM contribution occurs only in higher order and is negligibly small. The stopped kaon method was adopted and an elaborate detector system with a toroidal configuration was constructed to provide a substantial suppression of the systematic errors. A double ratio measurement was performed with respect to two opposite kinematic situations with π^0s going in the *forward* and in the *backward* directions. In the analysis, a unique method of a two-analysis combination was developed in order to reduce the ambiguity associated with the individual analyses. A total of 11.8×10^6 good $K_{\mu3}$ events were selected in the relevant π^0 angular regions. The results obtained are

$$P_T = -0.0017 \pm 0.0023(\text{stat}) \pm 0.0011(\text{syst})$$

$$\mathrm{Im}\xi = -0.0053 \pm 0.0071(\text{stat}) \pm 0.0036(\text{syst}).$$

By adding the statistical and systematic errors quadratically, one obtains $P_T = -0.0017 \pm 0.0026$ and $\mathrm{Im}\xi = -0.0053 \pm 0.0080$, which can be converted to 90% confidence limits of

$$|P_T| < 0.0050 \text{ (90\% C.L.)}$$

$$|\mathrm{Im}\xi| < 0.016 \text{ (90\% C.L.)},$$

improving the current limits for these quantities.

ACKNOWLEDGMENTS

[1] I. I. Bigi and A. I. Sanda, *CP Violation* (Cambridge University Press, Cambridge, England, 2000).

[2] G. Lüders, Dansk. Mat. Fys. Medd. **28**, 5 (1954); Ann. Phys. (Berlin) **2**, 1 (1957); W. Pauli, Nuovo Cimento **6**, 204 (1957).

[3] See, for example, the prologue of [1].

[4] J. H. Christensen *et al.*, Phys. Rev. Lett. **13**, 138 (1964).

[5] K. Abe *et al.* (Belle Collaboration), Phys. Rev. Lett. **87**, 091802 (2001); B. Aubert *et al.* (*BABAR* Collaboration), Phys. Rev. Lett. **87**, 091801 (2001).

[6] See, for example, J. M. Drake, E. G. Bilpuch, G. E. Mitchell, and J. F. Shriner, Phys. Rev. C **49**, 411 (1994), and references therein.

[7] See, for example, B. R. Holstein, *Weak Interactions in Nuclei* (Princeton University Press, Princeton, NJ, 1989), p. 112, and references therein.

[8] S. M. Barr and W. J. Marciano, in *CP Violation*, edited by C. Jarlskog (World Scientific, Singapore, 1999), p. 455.

[9] A. Angelopoulos *et al.* (CPLEAR Collaboration), Phys. Lett. B **444**, 43 (1998).

[10] P. K. Kabir, Phys. Rev. D **2**, 540 (1970).

[11] A. Alavi-Harati *et al.* (KTeV Collaboration), Phys. Rev. Lett. **84**, 408 (2000).

[12] L. Wolfenstein, Phys. Rev. Lett. **83**, 911 (1999); J. Ellis and N. E. Mavromatos, Phys. Rep. **320**, 341 (1999).

[13] P. Harris (EDM Collaboration), Plemiminary Result of SUSY-2005, Durham, 2005.

[14] B. C. Regan, E. D. Commins, C. J. Schmidt, and D. DeMille, Phys. Rev. Lett. **88**, 071805 (2002).

[15] M. V. Romalis, W. C. Griffith, J. P. Jacobs, and E. N. Fortson, Phys. Rev. Lett. **86**, 2505 (2001).

[16] T. Soldner *et al.*, Phys. Lett. B **581**, 49 (2004).

[17] R. Huber *et al.*, Phys. Rev. Lett. **90**, 202301 (2003).

[18] N. Danneberg *et al.*, Phys. Rev. Lett. **94**, 021802 (2005).

[19] S. R. Blatt *et al.*, Phys. Rev. D **27**, 1056 (1983).

[20] J. J. Sakurai, Phys. Rev. **109**, 980 (1958).

[21] I. I. Bigi and A. I. Sanda, in Ref. [1], p. 147.

[22] A. Riotto and M. Trodden, Annu. Rev. Nucl. Part. Sci. **49**, 35 (1999); M. Dine and A. Kusenko, Rev. Mod. Phys. **76**, 1 (2004).

[23] Y. Grossman, Int. J. Mod. Phys. A **19**, 907 (2004); T. Hurth, Rev. Mod. Phys. **75**, 1159 (2003).

[24] V. V. Anisimovsky *et al.* (E246 Collaboration), Phys. Lett. B **562**, 166 (2003).

[25] M. Abe *et al.* (E246 Collaboration), Phys. Rev. Lett. **93**, 131601 (2004).

[26] J. A. Macdonald *et al.*, Nucl. Instrum. Methods Phys. Res., Sect. A **506**, 60 (2003).

[27] N. Cabibbo and A. Maksymowicz, Phys. Lett. **9**, 352 (1964); **11**, 360(E) (1964); **14**, 72(E) (1965).

[28] S. Eidelman *et al.* (Particle Data Group), Phys. Lett. B 592, 1 (2004).

[29] R. M. Barnett *et al.* (Particle Data Group), Phys. Rev. D **54**, 1 (1996).

[30] G.-H. Wu, K. Kiers, and J. N. Ng, Phys. Rev. D **56**, 5413 (1997).

[31] M. Kobayashi, T.-T. Lin, and Y. Okada, Prog. Theor. Phys. **95**, 361 (1996).

[32] A. R. Zhitnitkii, Sov. J. Nucl. Phys. **31**, 529 (1980).

[33] V. P. Efrosinin *et al.*, Phys. Lett. B **493**, 293 (2000).

[34] A. I. Sanda, Phys. Rev. D **23**, 2647 (1981); N. G. Deshpande, Phys. Rev. D **23**, 2654 (1981); H.-Y. Cheng, Phys. Rev. D **26**, 143 (1982); **34**, 1397 (1986); I. I. Bigi and A. I. Sanda, Phys. Rev. Lett. **58**, 1604 (1987); M. Leurer, Phys. Rev. Lett. **62**, 1967 (1989); H.-Y. Cheng, Phys. Rev. D **42**, 2329 (1990).

[35] R. Garisto and G. Kane, Phys. Rev. D **44**, 2038 (1991).

[36] G. Bélanger and C. Q. Geng, Phys. Rev. D **44**, 2789 (1991).

[37] M. Fabbrichesi and F. Vissani, Phys. Rev. D **55**, 5334 (1997).

[38] G.-H. Wu and J. N. Ng, Phys. Lett. B **392**, 93 (1997).

[39] M. Leurer, Phys. Rev. Lett. **62**, 1967 (1989).

[40] K. Young *et al.*, Phys. Rev. Lett. **18**, 806 (1967); M. J. Longo, K. K. Young, and J. A. Helland, Phys. Rev. **181**, 1808 (1969).

[41] J. Sandweiss *et al.*, Phys. Rev. Lett. **30**, 1002 (1973).

[42] W. M. Morse *et al.*, Phys. Rev. D **21**, 1750 (1980).

[43] J. Imazato *et al.*, Proceedings of the 11th International Conference on Magnet Technology, Tsukuba, Japan, 1989.

[44] V. V. Lyuboshits, Sov. J. Nucl. Phys. **31**, 509 (1980); **32**, 362 (1980).

[45] A. Jodidio *et al.*, Phys. Rev. D **34**, 1967 (1986); **37**, 237(E) (1988).

[46] A. Schenck, *Muon Spin Rotation Spectroscopy* (Adam Hilger Ltd., Bristol, 1985), p. 112; S. Tanigawa *et al.*, Hyperfine Interact. **17–19**, 235 (1984).

[47] A muon beam facility at the 500 MeV proton booster synchrotron of KEK; K. Nagamine, Hyperfine Interact. **8**, 787 (1981).

[48] K. H. Tanaka *et al.*, Nucl. Instrum. Methods Phys. Res., Sect. A **363**, 114 (1995).

[49] M. P. Grigor'ev *et al.*, Instrum. Exp. Tech. **41**, 803 (1998).

[50] 3-D field calculation code using finite element method, Product of Vector Fields Ltd., Kidlington, Oxford, UK.

[51] A. P. Ivashkin *et al.*, Nucl. Instrum. Methods Phys. Res., Sect. A **394**, 321 (1997).

[52] D. V. Dementyev *et al.*, Nucl. Instrum. Methods Phys. Res., Sect. A **440**, 151 (2000).

[53] Yu. G. Kudenko *et al.*, Nucl. Instrum. Methods Phys. Res., Sect. A **411**, 437 (1998).

[54] T. Ikeda *et al.*, Nucl. Instrum. Methods Phys. Res., Sect. A **401**, 243 (1997).

[55] T. K. Ohska *et al.*, IEEE Trans. Nucl. Sci. **NS-33**, 98 (1986); Y. Arai, *ibid.* **NS-33**, 771 (1986).

[56] M. Nomachi *et al.*, Proceedings of the International Conference on Computing in High Energy Physics (CHEP94) (LBL Report No. LBL-358221, 1994), p. 114.

[57] M. Abe *et al.*, Phys. Rev. Lett. **83**, 4253 (1999).

[58] In the individual analysis A2 preceding the combination, the constant background level b was calculated simply from the integration from 12 to 19.5 μs, and N is the total counts up to 8 μs.

[59] P_T, P_N, and P_L are hereafter the average values in the region kinematically accepted by the muon stopper.

[60] Detector description and simulation tool, CERN library, http://wwwasdoc.web.cern.ch/wwwasdoc/pdfdir/geant.pdf.

[61] For Data III the check of A_N was omitted in this stage of the A1 individual analysis.

[62] Energy calibration was not used. About 90% of kaon stopped fiber events had more than 4096 ADC bin.

[63] C. H. Chen, C. Q. Geng, and C. C. Lih, Phys. Rev. D **56**, 6856 (1997).

[64] Recent data from G. Abbiendi *et al.* (OPAL Collaboration), Phys. Lett. B **520**, 1 (2001) and R. Barate *et al.* (ALEPH Collaboration), Eur. Phys. J. C **19**, 213 (2001) were applied to the analysis of

Y. Grossman, Nucl. Phys. **B426**, 355 (1994).

[65] The results of Wu and Ng [38] were criticized in [37] as relying upon some accidental precise cancellations between chargino contributions with gluino amplitudes.

[66] D. Ambrose *et al.*, Phys. Rev. Lett. **81**, 5734 (1998).

[67] KEK Report No. 99-4, 1999.

[68] W.-F. Chang and J. N. Ng, hep-ph/0512334.